Functional and Molecular Photoacoustic Computed Tomography Using Light Emitting Diodes

Sumit Agrawal and Sri Rajasekhar Kothapalli

Abstract Photoacoustic Computed Tomography (PACT) has been widely explored for inexpensive non-ionizing functional and molecular imaging of small animals and humans. In order for light to penetrate into deep tissue, a bulky and high-cost tunable laser is typically employed. Light Emitting Diodes (LEDs) have recently emerged as smaller and cost-effective alternative illumination sources for photoacoustic (PA) imaging. We recently developed a portable, low-cost multispectral three-dimensional PACT system using multi-wavelength LED arrays, referred to as LED-PACT, enabling similar functional and molecular imaging capabilities as standard tunable lasers. In this chapter, first the capabilities of commercial LED array-based B-mode PA and Ultrasound (US) imaging system, referred to as LED-PAUS, to perform functional and molecular imaging with both in vivo and phantoms studies are presented. We also present the details of the development of LED-PACT system with essential hardware components, acquisition and reconstruction software needed for the implementation. This chapter also covers simulations and experimental results comparing the capabilities of LED-PACT system with commercial LED-PAUS system. LED-PACT and LED-PAUS system together demonstrate the potential of LED based photoacoustic imaging for pre-clinical and clinical applications.

1 Introduction

Photoacoustic tomography (PAT) is an emerging biomedical imaging technology that combines rich optical contrast with the high spatial resolution of ultrasound [1, 2]. In PAT, a biological specimen is illuminated with a sufficiently short laser pulse, which

S. Agrawal (✉) · S. R. Kothapalli
Department of Biomedical Engineering, Pennsylvania State University, University Park, State College, PA 16802, USA
e-mail: sua347@psu.edu

S. R. Kothapalli
Penn State Cancer Institute, Hershey, PA 17033, USA
e-mail: srkothapalli@psu.edu

M. Kuniyil Ajith Singh (ed.), *LED-Based Photoacoustic Imaging*,
Progress in Optical Science and Photonics 7,
https://doi.org/10.1007/978-981-15-3984-8_11

causes an increase in temperature due to energy absorption. This temperature increase leads to thermoelastic expansion of the specimen, which induces ultrasonic pressure generation. The generated pressure then propagates to transducers surrounding the specimen. The received ultrasound signal is converted into an optical-absorption map of the specimen with different image formation methods. PAT has shown great potential in biomedicine for several applications ranging from clinical breast angiography [3, 4] to pre-clinical whole body imaging of small animals [5–7].

Based on the image formation methods, PAT setups can be grouped into two major categories. In the first method, a single element transducer mechanically scans the imaging object in two dimensions. Photoacoustic received signal at each acquisition provides a one-dimensional image along the acoustic focus of the transducer element. Elementary stitching of these one-dimensional images along the two dimensions of the mechanically scanned region of interest gives a three-dimensional optical absorption map of the specimen. PAT setups using this direct method of image formation are called as photoacoustic microscopy (PAM) setups [8–10]. In the second method, different geometries of multi-element transducer arrays are used to electronically scan the imaging object. Each element of the transducer has a larger acceptance angle compared to the previous case. Photoacoustic image formation involves complex computational reconstruction algorithms that can effectively merge the data from all transducer elements. PAT setups using these complex reconstruction methods are called as photoacoustic computed tomography (PACT) setups [11–15].

Common PACT setups comprise of a cumbersome Q-switched Nd:YAG laser [11–15]. These lasers typically have a nanosecond pulse width with hundreds of mJ pulse energy. Such high pulse energies can easily provide sufficient signal to noise ratios for applications ranging from organelles to small animals to human imaging. However, these laser sources, widely explored in a typical research setup, are not suitable for clinical applications due to their massive cost and substantial footprints.

Recently, many researchers have employed both laser diodes [16–22] as well as LEDs [22, 23] in the development of PA imaging systems. However, the emission from laser diodes still remain coherent and are still under the category of class-IV lasers. LEDs, unlike the class-IV lasers, offer a unique opportunity to operate with more flexibility and ease of use. The challenging aspect of using LEDs compared to laser sources for PA imaging is their low power pulses (about two orders of magnitude smaller than the typical class-IV lasers) struggling to provide sufficient signal from deeper tissue regions. To overcome this, sizable signal averaging is performed utilizing the orders of magnitude higher repetition rates of the LEDs.

Several groups have explored the LED based PA imaging applications utilizing the higher repetition rates to achieve acceptable signal to noise ratios. Further, to improve the pulse energies researchers have also explored the arrayed arrangement of LEDs [24–29]. In the arrayed format, the typical pulse energies increases from few μJ to hundreds of μJ and thus improves the penetration depth of LED-based PA imaging.

The previous studies [24–29] utilized the arrayed format of LED arrays only in a typical B-mode fashion, where they place two LED arrays adjacent to a linear ultrasound probe and acquire B-mode photoacoustic images along the depth dimension

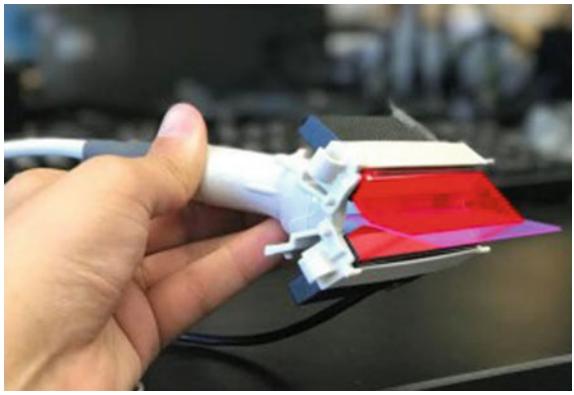

Fig. 1 LED arrays attached to conventional ultrasound probe [Reprinted with permission from 24]

of the specimen. There are two disadvantages of using the LED arrays in the above format. First, in order for light and ultrasound to fall in the common imaging plane, the angled arrangement of LED arrays (as shown in Fig. 1) leads to a standoff region of about 8–10 mm.

Second, for deep tissue imaging applications, the signal to noise ratio reduces drastically with the lower light energy reaching to the deeper regions. We have addressed the above-mentioned problems with a novel approach of placing multiple LED arrays around the imaging specimen. Our setup not only provides a close-to-zero standoff region but also helps to increase the penetration depths in deep tissue imaging applications to about 35 mm, similar to the big lasers.

With this approach, ours is the first LED based three-dimensional PACT system that uses multiple LED arrays and a linear ultrasound probe to generate volumetric 3-D PACT images of the imaging object. Similar to the high-cost tunable lasers, our LED-PACT system allows for the multi-wavelength LED arrays housed in a cylindrical geometry to enable the functional and molecular imaging capabilities.

The rest of the chapter is organized as follows. Section 2 presents several phantom as well as in vivo studies demonstrating the capabilities of the commercial LED-PAUS system. Section 3 first describes our proposed LED-PACT system with the details of the development of the hardware as well as the reconstruction of PACT images. It also presents simulations and validation studies over different tissue mimicking phantoms comparing the capabilities of our proposed system with the LED-PAUS system and proposing solutions to overcome its limitations towards the goal of developing a clinically applicable, low-cost LED-PACT system.

2 LED-Based PAUS Imaging

The commercially available LED-based combined ultrasound (US)/photoacoustic (PA) B-mode imaging system, referred to as LED-PAUS system, explained below

in Sect. 2.1 is capable of acquiring 2-D/3-D B-mode US/PA images in real time. In this section, we first introduce the commercially available LED based PAUS system and then present different studies involving LED based PAUS system.

2.1 Commercial LED-PAUS Imaging System

A commercially available LED-PAUS system (AcousticX, Cyberdyne Inc., Ibaraki, Japan) capable of acquiring interleaved PA and US B-mode images in real time was presented previously [26, 27]. This system uses LED arrays for PA excitation and a linear US transducer for ultrasonic excitation and detection. For B-mode 2-D/3-D US/PA acquisition, two LED arrays are positioned on either side of the US probe as shown in Fig. 1. Each of these LED arrays consists of four rows of 36 1 mm × 1 mm LEDs. These LED arrays are capable of delivering a maximum optical energy of 200 μJ per pulse and can be driven with a repetition rate of 1–4 kHz with pulse duration of 30–150 ns. The ultrasound probe is a lead zirconate titanate (PZT) 128-element linear array transducer having a pitch of 0.3 mm and total length of 38.4 mm. The central frequency of the transducer is 7 MHz and the measured −6 dB bandwidth is 75%. The ultrasound and photoacoustic modalities have sampling rates of 20 MHz and 40 MHz respectively. The US probe has an elevation focus of 15 mm, achieved with the help of an acoustic lens incorporated on top of the transducer array. In the following subsections, we have covered several phantom as well as in vivo studies published using this LED-PAUS system.

2.2 Capability of LED-PAUS System to Image Exogenous Contrast Agents

Exogenous contrast agents can be targeted for specific molecules or cells for preclinical and clinical applications. Photoacoustic contrast agents have significant feasibility to assist in monitoring and diagnosis of diseases [30–36]. This work from Hariri et al. [24] characterized the detection limit of some common small molecules used in photoacoustic imaging: ICG [31], MB [32, 33], and DiR [36]. These are NIR-sensitive, Food and Drug Administration (FDA)-approved contrast agents for both Fluorescent and photoacoustic imaging. Various concentrations were scanned, and the detection limits were calculated at three standard deviations above baseline. Figure 2a, e, i show MIP images of high concentrations of ICG (640, 320, and 160 μM), MB (6, 3, and 1.5 mM), and DiR (592, 296, and 148 μM). Figure 2b, f, j shows the average photoacoustic intensity along all ten ROIs for each tube associated with Fig. 2a, e, i.

Figure 2c, g, k show MIP images for the detection limit of ICG (36, 18, 9 μM, and DI water), MB (1.5, 0.75, 0.37 mM, and DI water), and DiR (136, 68, 34 μM, and DMSO). Figure 2d, h, l show the average photoacoustic intensity along the ROIs.

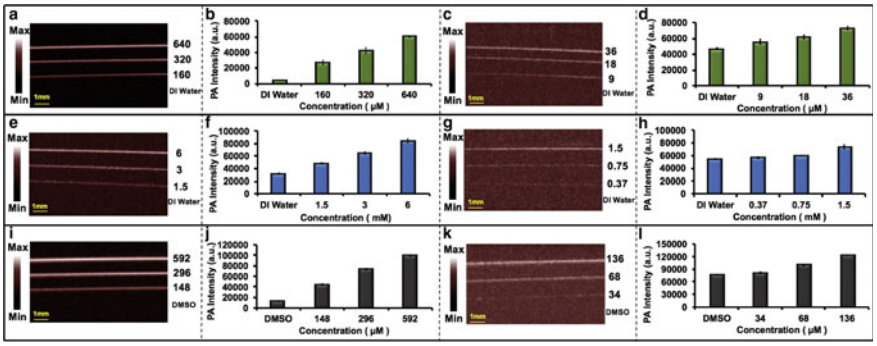

Fig. 2 Evaluation of LED-based photoacoustic imaging system for exogenous contrast agents. **a** MIP image of ICG solutions (640, 320, 160 μM, and DI water) with high concentration as positive control inside Teflon light wall tubes. **b** Statistical analysis of data in A. **c** MIP image detection limit experiment for ICG (36, 18, 9 μM, and DI water). **d** Statistical analysis of data in (**c**). **e** MIP images of MB solutions (6, 3, 1.5 mM, and DI water) with high concentration as positive control inside Teflon light wall tubes. **f** Statistical analysis of data in (**e**). **g** MIP image detection limit experiment for MB (1.5, 0.75, 0.37 mM, and DI water). **h** Statistical analysis of data in (**g**). **i** MIP images of DiR solutions (592, 320, 148 μM, and DMSO) with high concentration as positive control inside Teflon light wall tubes. **j** Statistical analysis of data in (**i**). **k** MIP image detection limit experiment for DiR (136, 68, 34 μM, and DMSO). **l** Statistical analysis of data in (**k**). All the error bars demonstrate standard deviation between different ROIs in each tube. Scan size is 10 mm [Reprinted with permission from 24]

The error bars show the standard deviation between ROIs in each tube. The limit of detection for ICG, MB, and DiR is 9 μM, 0.75 μM, and 68 μM, respectively when 850 nm is used for ICG and DiR and 690 nm is utilized for MB. The power for the LED-based system at 690 nm is almost three-fold lower than that at 850 nm. This might explain the lower detection limit for MB rather than ICG and DiR. This experiment also highlights how LED based systems are limited by the choice of wavelengths. While OPO based systems are capable of scanning wide-wavelength range, this system can only use two wavelengths at a time. Thus, it can be challenging to carefully match the absorption peak of the contrast agent with the excitation source. Nevertheless, many species absorb strongly at 690 or 850 nm and customized LED sets are available for ratiometric imaging.

2.3 Capability of LED PAUS System to Image Labeled Cells in Vivo

This work from Hariri et al. [24]. presents in vivo experiments to demonstrate the feasibility of LED-PAUS system for clinical applications. Several groups [37, 38] have previously used photoacoustic imaging for stem cell imaging. Here, labeled cells are used to understand the in vivo performance of this LED-PAUS system. This

study used DiR which has been demonstrated as an effective contrast agent for cells checking [39, 40]. Figure 3a, e, i show photoacoustic images before injection of DiR, DiR @ HMSC, and HMSC, respectively.

The needle generates strong photoacoustic signal and overlaying the photoacoustic data with the ultrasound images offers more comprehensive structural information in addition to functional details from DiR-labeled cells. Figure 3b, f, J demonstrate B-mode photoacoustic/ultrasound images before injection. Figure 3c, d shows photoacoustic and photoacoustic/ultrasound images of injected DiR in the mice, respectively. These figures show strong photoacoustic signal in the presence of DiR. Figure 3g shows capability of LED-PAUS system to detect cells labeled with contrast agent. DiR was used as contrast agent for labeling the HMSCs. Unlabeled HMSCs

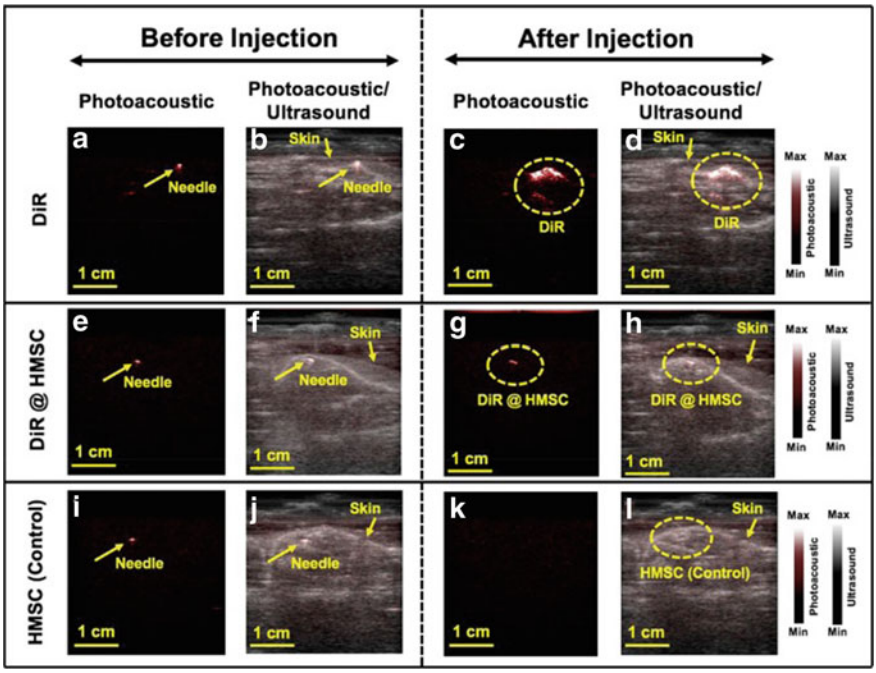

Fig. 3 In vivo evaluation of LED-PAUS system. **a** Photoacoustic image when needle is subcutaneously injected on spinal cord area before DiR injection. The needle has strong photoacoustic signal. **b** Photoacoustic/ultrasound image of (**a**). **c** Photoacoustic image after subcutaneously injection of DiR. **d** B-mode photoacoustic/ultrasound image of (**c**). **e** Photoacoustic image when needle is subcutaneously placed on the spinal cord area before HMSC labeled with DiR (DiR @ HMSC) injection. **f** B-mode photoacoustic/ultrasound image of (**e**). **g** Photoacoustic image after injection of HMSC labeled with DiR (DiR @ HMSC) on spinal cord. **h** B-mode photoacoustic/ultrasound image of (**g**).**i** Photoacoustic image in presence of needle before injection of unlabeled HMSC as control experiment. **j** B-mode photoacoustic/ultrasound image of (**i**). **k** Photoacoustic image of HMSC as control. This image shows no photoacoustic signal for HMSC. **l** B-mode photoacoustic/ultrasound image of (**k**). [Reprinted with permission from 24]

were also injected as control (Fig. 3k, l), but there was no increase in photoacoustic signal. Hence this study demonstrated the feasibility of LED-PAUS system for in vivo studies including photoacoustic cell imaging.

2.4 LED-PAUS System for Monitoring Angiogenesis in Fibrin Scaffolds

Laser speckle contrast analysis (LASCA), a widely used imaging technique within regenerative medicine, has high spatial resolution but offers limited imaging depth and is only sensitive to perfused blood vessels. As an emerging technology, PA imaging can provide centimeters of imaging depth and excellent sensitivity in vascular mapping. PA imaging in combination with conventional US imaging offers a potential solution to this challenge in regenerative medicine. This study from Zhu et al. [41] presented here used LED-PAUS dual system to image and monitor angiogenesis for 7 days in fibrin-based scaffolds subcutaneously implanted in mice. Scaffolds, with or without basic fibroblast growth factor (bFGF), were imaged on day 0 (i.e., post implantation), 1, 3, and 7 with both LASCA and LED-PAUS imaging systems. Quantified perfusion measured by LASCA and PA imaging were compared with histologically determined blood vessel density on day 7. Vessel density corroborated with changes in perfusion measured by both LASCA and PA. Unlike LASCA, PA imaging enabled delineation of differences in neovascularization in the upper and the lower regions of the scaffold. Overall, this study has demonstrated that PA imaging could be a noninvasive and highly sensitive method for monitoring vascularization at depth in regenerative applications.

2.4.1 In Situ Polymerization of Fibrin Scaffolds

This in vivo research [41] was conducted with the approval of the Institutional Animal Care and Use Committee at the University of Michigan. Female BALB/c mice ($n = 5$, 19.2 ± 1.0 g, 4–6 weeks old; Charles River Laboratories, Wilmington, MA) were anesthetized with isoflurane (5% for induction and 1.5% for maintenance). The lower dorsal hair was removed by shaving and applying depilatory cream (Nair, Church & Dwight Co, Ewing, NJ). The skin was disinfected with povidone-iodine (Betadine, Purdue Products L.P., Stamford, CT). The scaffold mixture (0.3 mL per implant) was injected subcutaneously using a 20-gauge needle (Becton Dickinson, Franklin Lakes, NJ) at two locations within the lower dorsal region and allowed to polymerize for 2 min before removal of the needle. The scaffold mixture consisted of the following: 10 mg/mL bovine fibrinogen (Sigma-Aldrich, St. Louis, MO) in Dulbecco's modified Eagle's medium (Life Technologies, Grand Island, NY), 0.05 U/mL bovine aprotinin (Sigma-Aldrich), 125 μg/mL Alexa Fluor 647-labeled human

fibrinogen (Molecular Probes, Eugene, OR), 2 U/mL bovine thrombin (Thrombin-JMI, King Pharmaceuticals, Bristol, TN), 34 μg/mL bovine serum albumin (Sigma-Aldrich), and 6.6 mU/mL porcine heparin (EMD Millipore, Burlington, MA). Each mouse received one implant with 1 μg of bFGF (EMD Millipore) per scaffold, whereas the contralateral implant served as a negative control (i.e., 0 mg bFGF). The placement of the negative control (i.e., left or right side) was randomized in all mice.

2.4.2 LASCA and LED-PAUS Imaging of Scaffolds

The detailed experimental schedule, including scaffold implantation and imaging, is shown in Fig. 4. On days 2, 4, and 6, 50 μL of 20 μg/mL bFGF was subcutaneously injected into scaffolds initially containing bFGF on day 0 (i.e., +bFGF). Phosphate buffered saline (Life Technologies) was injected into the negative control scaffolds (i.e., −bFGF). LASCA and PA imaging procedures were done in no particular order on days 0, 1, 3, and 7. A brief schematic diagram of LASCA/PA imaging is also shown in Fig. 4. After the completion of imaging on day 7, the mice were euthanized, and the implants were retrieved for histology.

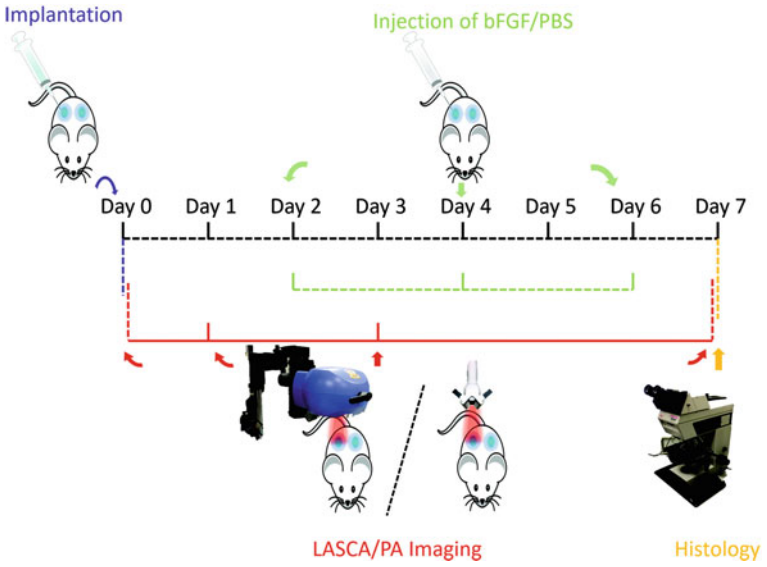

Fig. 4 The 7-day longitudinal experimental schedule. Scaffold implantation was done on day 0. LASCA/PA imaging was on day 0 (i.e., after implantation), 1, 3, and 7. bFGF or PBS was injected subcutaneously adjacent to each scaffold every 2 days. Scaffolds were retrieved on day 7 for H&E and CD31 staining. Each mouse received two scaffolds represented by the blue areas. bFGF, basic fibroblast growth factor; H&E, hematoxylin and eosin; LASCA, laser speckle contrast analysis; PA, photoacoustic; PBS, phosphate buffered saline [Reprinted with permission from 41]

LASCA imaging was employed to monitor the perfusion noninvasively and longitudinally in and around the subcutaneous implants placed in the lower dorsal region. To perform LASCA imaging, the mice were anesthetized with isoflurane and imaged with a PeriCam PSI HR (Perimed, Ardmore, PA) LASCA system. Figure 5a displays a macroscopic image of a mouse with implants along with longitudinal perfusion images from days 0 to 7. The ROIs are marked by black and red ellipses, indicating the −bFGF and +bFGF implants, respectively. The LASCA images qualitatively show more perfusion in the +bFGF scaf- folds than the −bFGF scaffolds in the days after implantation. Figure 5b shows a quantitative analysis of the ROIs, which was based on computing a relative change in average perfusion units for a given implant relative to day 0. Overall perfusion tended to increase over time, with the greatest increase observed for the +bFGF group relative to the −bFGF group, which approached statistical significance on day 7 ($p = 0.055$).

To perform LED-PAUS imaging, mice were anesthetized with isoflurane and secured to a platform in a prone position. The platform was partially submerged in a 37 °C water tank such that the implanted scaffolds were completely submerged for imaging. Two 850 nm LED arrays were used for imaging. A series of 2-D US and PA images of each scaffold were acquired at 10 Hz in the sagittal orientation while the probe was translated at 0.5 mm/s across the volume of the implant. Figure 6a

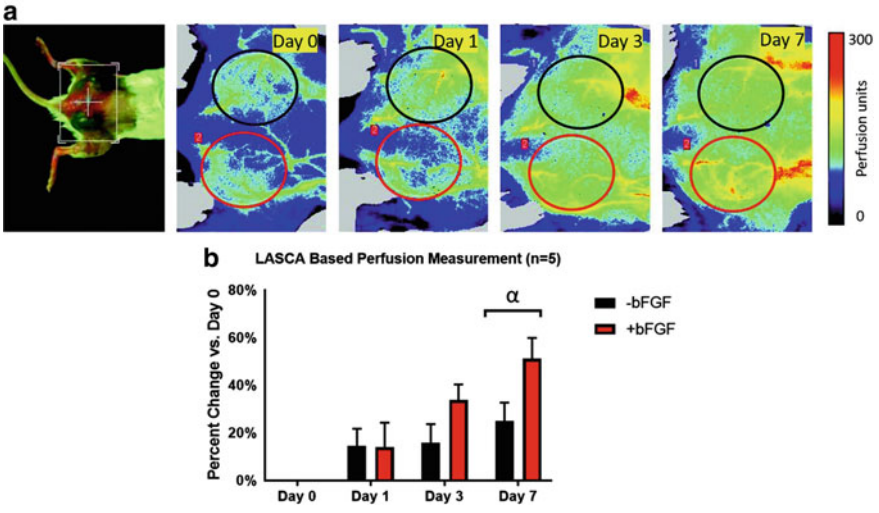

Fig. 5 **a** Photo of dorsal view (leftmost) and longitudinal LASCA images of a mouse with two subcutaneous implants. The ROIs were chosen based on the physical location of the implants, and are denoted by colored ellipses (red for +bFGF and black for −bFGF). For all LASCA images, the caudal direction is toward the left. ROI dimensions: 1.1 cm (major axis), 1.0 cm (minor axis). **b** Quantification of the change in perfusion relative to day 0, based on an ROI analysis of the LASCA images, shows an overall increase in perfusion over time. The greatest change in perfusion was observed on day 7, with +bFGF scaffolds trending toward greater perfusion than −bFGF scaffolds. α: −bFGF versus +bFGF on day 7 ($p = 0.055$). ROIs, regions of interest [Reprinted with permission from 41]

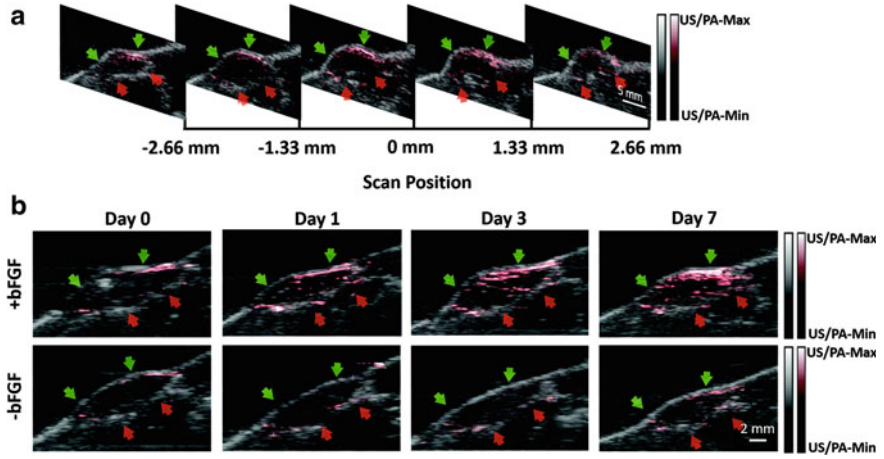

Fig. 6 Longitudinal LED-PAUS imaging of two subcutaneous implants. Green and red arrows indicate the upper and lower edges of the scaffold, as determined through the B-mode US. **a** A series of two-dimensional PAUS images from a +bFGF scaffold on day 7 at different scan positions. Note that only images within the range of −2.5 to 2.5 mm are used for MIP image. **b** A series of longitudinal MIP PAUS images of +bFGF and −bFGF scaffolds from the same mouse. PA intensity represented in red has the greatest difference on day 7. MIP, maximum intensity projected; US, ultrasound [Reprinted with permission from 41]

shows a series of 2-D PAUS images from a +bFGF scaffold on day 7 at different scan positions (i.e., sagittal planes). The PA signal, in red, is overlaid on the B-mode US image, in grayscale. Figure 6b shows a series of longitudinal MIP PAUS images of both scaffolds from the same mouse. Qualitatively, the +bFGF implant has a PA intensity that increased over time, especially adjacent to the skin. Some signal appears within the scaffold, likely due to the projection of multiple images into a single plane. With the −bFGF implant, only point-like contrast was detected in the scaffold, with no obvious trend during the 7-day experiment. The PA signal from the +bFGF and −bFGF scaffolds appeared similar on day 0. The results on different days of each mouse are normalized with day 0 and then compared the percentage change. The greatest difference was observed on day 7, which was also consistent with the LASCA results. On day 7, the +bFGF scaffold displayed a strong PA signal, especially between the skin and upper layer of the implant. Some PA signal was observed in the −bFGF scaffold, although at a lower level compared with the +bFGF scaffold.

Further, the perfusion in implants measured by both LASCA and LED-PAUS imaging techniques were validated by quantitative histology. Imaging was able to cover the entire scaffold volume, and enabled delineation of neo-vascularization in the upper and the lower regions of the scaffolds, respectively. The LED-PA imaging results well matched with the findings from histology, suggesting that PA imaging could be a non-invasive and highly sensitive method for monitoring angiogenesis at depth in regenerative applications.

2.5 *High Speed Photoacoustic Imaging Using LED-PAUS System*

Conventional laser-based PA imaging systems are not suitable for dynamic studies because of their low repetition rates and consequent low frame rates. LED's used in LED-PAUS system can be driven at high repetition rates of upto 4 kHz, offering the possibility of real-time PAUS imaging at frame rates close to 30 Hz. However, this frame rate is still not enough for applications involving dynamic tissue movements. This study from Sato et al. [42], presents a new high-speed (HSS) imaging mode in the LED-PAUS system. In this mode, instead of toggling between ultrasound and photoacoustic measurements, it is possible to continuously acquire only photoacoustic data for about 1.5 s with a time interval of 1 ms. With this improvement, photoacoustic signals can be recorded from the whole aperture (38 mm) at fast rate and can be reviewed later at different speeds for analyzing dynamic changes in the photoacoustic signals. This new high-speed feature opens up a feasible technical path for multiple dynamic studies that require high frame rates such as monitoring circulating tumor cells, voltage sensitive dye imaging, myocardial functional imaging etc.

This study validated the HSS mode by dynamically imaging the blood reperfusion in the finger of a human volunteer, thereby enabling the real-time measurement of the blood flow velocity. A rubber band was wrapped around the index finger, and the blood was pushed out as far as possible from the fingertip, causing temporary ischemia (Fig. 7a). Figure 7b shows the position of LED arrays on both sides of the US linear array probe and the finger placed between them. The finger and the LED-PAUS probe were positioned in a water bath as shown in Fig. 7c. After blocking the blood flow to the finger (by using rubber bands as shown in Fig. 7a), HSS mode was initiated and data acquisition was started. At the same instant, the rubber band wrapped around the finger was released in such a way that high-speed PA imaging can visualize the reperfusion of blood in the finger. To improve SNR, they pulsed the LED light source at 4 kHz and received the PA signal once every 0.25 ms. Four frames were averaged on board for improving SNR. To maintain high framerate, plane wave US imaging was used along with PA imaging. In addition, number of pulse-echo ultrasonic acquisitions was reduced to six frames to enable continuous

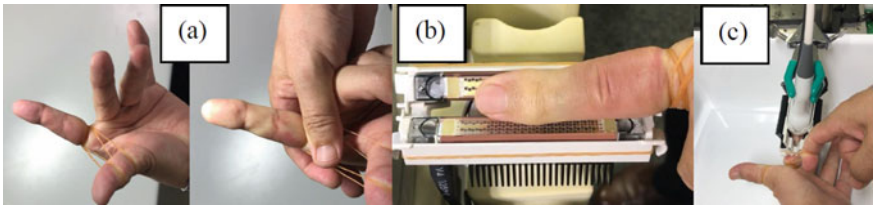

Fig. 7 **a** Rubber band used to block the blood flow to the finger, **b** positioning of finger and the LED-PAUS probe, **c** photograph of the probe and finger positioned inside the water bath [Reprinted with permission from 42]

high-speed PA signal acquisition for 1.5 s. Several measurements were done on the same finger of the volunteer to validate and evaluate the new high-speed imaging capability.

Figure 8 shows the results (first experiment) of imaging blood reperfusion in a human finger. Figure 8a shows the PA/US image at the start of acquisition, when there is almost no blood flow to the finger. Figure 2b–n shows the PA/US images at different time points (interval of 10 ms) during the high-speed acquisition. After the rubber band was released from the finger, PA signal intensity is clearly increasing in a blood vessel inside the imaging plane. It is visible that the blood vessel of interest is completely reperfused in about 130 ms.

Figure 9 shows the results of another example in which blood flow velocity is calculated from the reperfusion of blood in finger. The distance indicated by the dashed line was 6.4 mm, and the time taken for the blood to flow from the start point on the left side to the end on the right side was 35 ms. From this, blood flow was calculated to be about 18 cm/s.

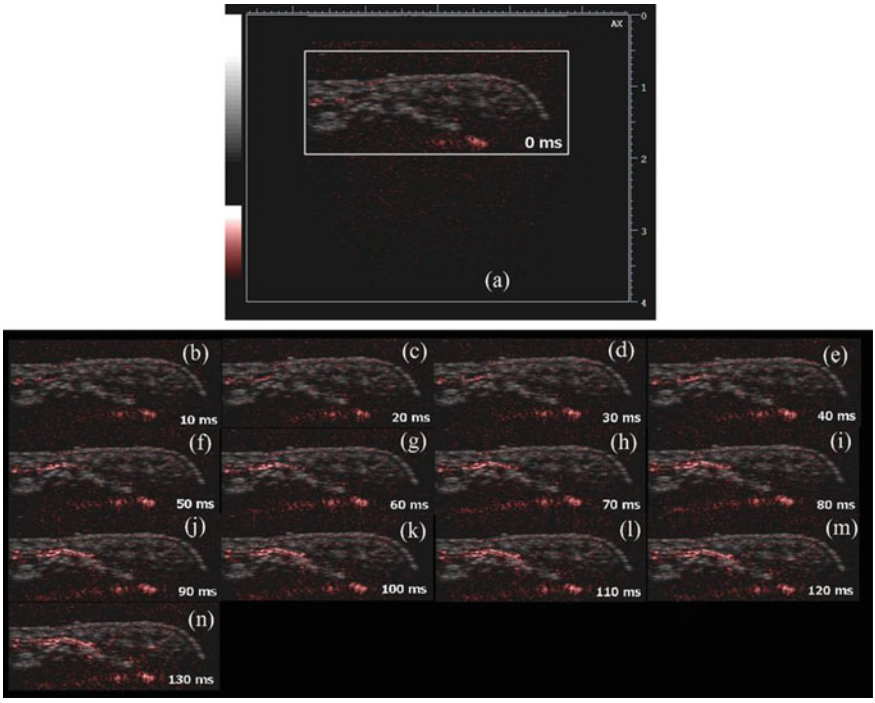

Fig. 8 LED-PAUS overlay images acquired and displayed at different time points during the reperfusion of blood vessel in a human finger. PA images are displayed in hot colormap and conventional US images are displayed in gray scale. It is clear from the images that blood is reperfused into one of the blood vessels as the time is increasing from 0–130 ms. By 130 ms, the blood vessel was completely reperfused [Reprinted with permission from 42]

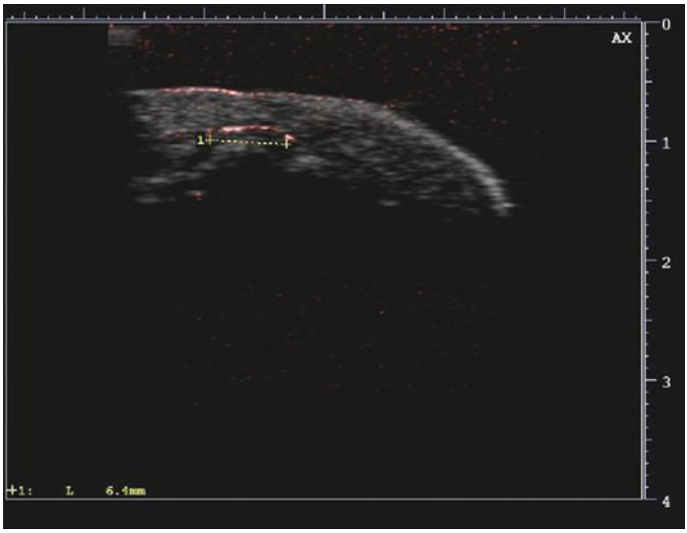

Fig. 9 LED-PAUS overlay image showing the reperfused blood vessel. Yellow line (indicated between '+' markers) shows the blood vessel from which the blood flow velocity was calculated [Reprinted with permission from 42]

2.6 Human Placental Vasculature Imaging Using LED-PAUS System

Minimally invasive fetal interventions, such as those used for therapy of twin-to-twin transfusion syndrome (TTTS), require accurate image guidance to optimize patient outcomes. Currently, TTTS can be treated fetoscopically by identifying anastomosing vessels on the chorionic (fetal) placental surface, and then performing photocoagulation. Incomplete photocoagulation increases the risk of procedure failure. Photoacoustic imaging can provide contrast for both haemoglobin concentration and oxygenation, and in this study, it was hypothesised that it can resolve chorionic placental vessels.

In this study, from Maneas et al. [43], to investigate the feasibility of the system to visualize superficial and subsurface placental vessels on the fetal chorionic placenta, a normal term placenta was collected with written informed consent after a caesarean section delivery at University College London Hospital. The umbilical cord was clamped immediately after the delivery to preserve the blood inside the vessels. The placenta was initially placed in a plastic container and subsequently it was coated with ultrasound gel for acoustic coupling and covered with cling film. The container was filled with water at room temperature for acoustic coupling and for free translation of the imaging probe. The experimental setup can be seen in Fig. 10.

LED-PAUS system with two 850 nm LED arrays was used to image several highly vascularized locations on the surface of the chronic fetal side. The linear stage was used to translate the imaging probe for 3-D image volume acquisition

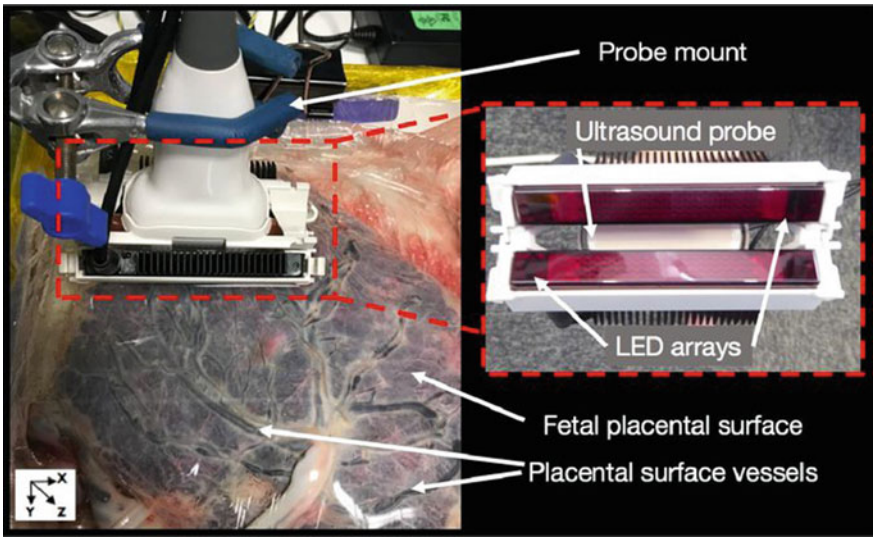

Fig. 10 Experimental setup to image a human placenta. A clamp was used to mount the ultrasound probe with the light emitting diode (LED) arrays to the linear motorized stage. The placenta was coated with ultrasound gel, covered with cling film, and placed inside a water-filled container [Reprinted with permission from 43]

along 40 mm scan region. Sample PA and US frames of a term human chorionic placental vasculature that were acquired in real-time are presented in Fig. 11. With PA imaging, superficial blood vessels and a subsurface structure were visible to a depth of approximately 5 mm from the placental chorionic fetal surface.

Some of these vascular structures were not apparent in US images. With US imaging, a large blood vessel located at a depth of approximately 7 mm could be identified, but this vessel was not apparent with PA imaging.

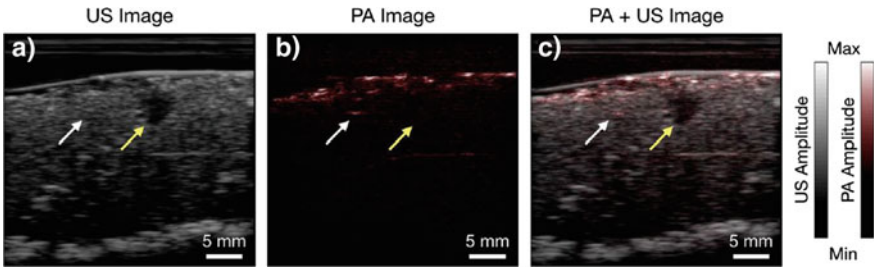

Fig. 11 Single frames of ultrasound (US), photoacoustic (PA), and merged US and PA images acquired from a human placenta, at one location (**a**–**c**). A large blood vessel (yellow arrow) that is visible in the US image was not visible in the PA image. A subsurface structure was visible with PA imaging (white arrow). All the images are displayed on logarithmic scales [Reprinted with permission from 43]

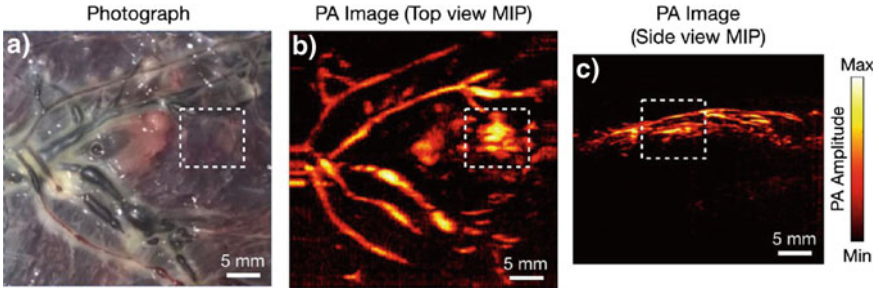

Fig. 12 Photograph (**a**) and photoacoustic (PA) images (**b**, **c**) of a portion of the human placenta. Superficial branching blood vessels are apparent in both the photograph and the PA images. High intensity PA signals (dashed squared box) that are not visible in the photograph might be attributable to subsurface vascular structures. The PA images are displayed on a logarithmic scale as maximum intensity projections (MIPs) of the reconstructed 3D photoacoustic image volume [Reprinted with permission from 43]

Figure 12 shows a photograph of the area that was imaged and the corresponding top and side maximum intensity projections (MIPs) of the reconstructed 3-D photoacoustic signals. Several superficial branching vessels were clearly resolved. In the top view MIP PA image, high intensity PA signals appeared to originate from vascular structures that were not visible in the photograph.

This feasibility study demonstrated that photoacoustic imaging can be used to visualize chorionic placental vasculature, and that it has strong potential to guide minimally invasive fetal interventions.

2.7 In Vivo Real-Time Oxygen Saturation Imaging Using LED-PAUS System

In this study, from Singh [44], potential of LED-based PAUS system in real-time oxygen saturation imaging is demonstrated using an in vivo measurement on a human volunteer. 2-D PA, US, and oxygen saturation imaging were performed on the index finger of a human volunteer. Results demonstrate that LED-based PAUS imaging system used in this study is promising for generating 2-D/3-D oxygen saturation maps along with PA and US images in real-time. Light illumination was provided by two combination LED arrays fixed on both sides of the US probe as shown in Fig. 13. Each LED arrays consists of 144 elements arranged in four rows. In this study, combination LED array were used in which first and third rows are embedded with 850 nm LED elements and second and fourth with 750 nm elements. For each LED array, energy per pulse is 50 μJ, and 100 μJ for 750 nm and 850 nm respectively. Light pulse duration can be varied from 30 to 100 ns and 70 ns pulse-width was used for the reported measurement.

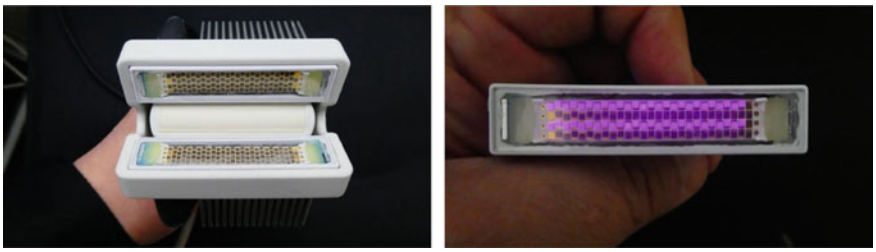

Fig. 13 Photograph of LED-based PAUS probe in which two LED arrays (750/850 nm) are placed on both sides of a linear array US probe (7 MHz) (left). Photograph of the LED array (right) with four rows of LED elements in which row 1 and 3 are 850 nm elements, row 2 and 4 are 750 nm elements. In this picture, 850 nm elements are activated and captured using an IR camera [Reprinted with permission from 44]

The system can pulse the LED arrays as well as transmit/acquire data parallel from all 128 elements of the US probe to generate interleaved PA/US (planewave or line-by-line) images at a frame rate of 30 Hz. System can drive the LED's at a rate of 4 kHz, providing the opportunity to average multiple frames without losing the frame rate. In the multispectral mode for oxygenation imaging, it can toggle between two wavelengths (750 and 850 nm in this case) at a rate of 4 kHz and provide oxygen saturation image overlaid with US or PA images at frame rates as high as 30 Hz.

Index finger of a human volunteer was immersed in water (imaging plane/location is marked in Fig. 14) and LED-PAUS probe was used to perform real-time (Frame rate: 10 Hz) interleaved oxygen saturation and US imaging. Real-time feedback allowed to align the probe with a pulsating radial artery (depth: 7 mm).

Figure 14 (right) shows the results of oxygenation imaging experiment using LED-PAUS system, in which tissue oxygenation map is overlaid on conventional US image. Alignment of probe was done in such a way that a pulsating radial artery was inside the imaging plane (this was verified using the pulsating nature of it while looking at one wavelength PA image). In the oxygenation image, arterial blood is visualized in red

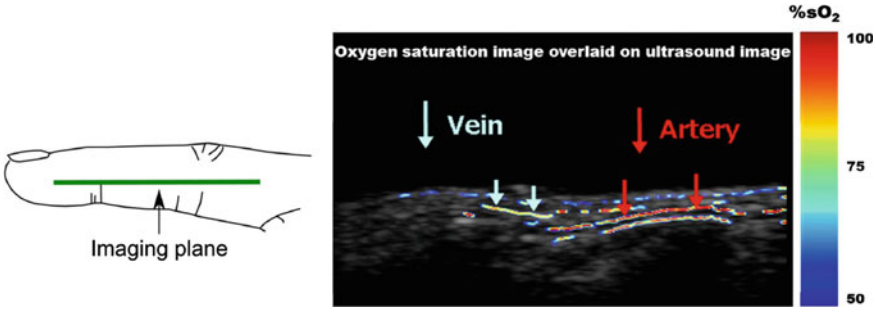

Fig. 14 Location on human finger where imaging was performed (left) and oxygen saturation image overlaid on conventional pulse echo image (right) [Reprinted with permission from 44]

color (oxygenation level close to 100%) and superficial venous blood in yellow shade (oxygenation level close to 70–75%) as expected. Also, it is interesting to see that skin melanin is visualized in blue color (above venous structure). It is commendable to mention that the system is capable to separate and visualize three different optical absorbers in tissue (arterial blood, venous blood, and melanin) using a simple 2 wavelength approach. It is important to note that, obtained oxygenation values are relative because of wavelength-dependent light fluence variations. However, form these results, it is clear that LED-PAUS system can differentiate arteries and veins in healthy human volunteers, where blood oxygenation changes in arterial and venous blood is expected to be less than around 20%.

2.8 In Vivo Imaging of Human Lymphatic System Using LED-PAUS System

Non-invasive in vivo imaging of lymphatic system is of paramount importance for analyzing the functions of lymphatic vessels, and for investigating their contribution to metastasis. This study from Singh [45] demonstrates the capabilities of LED-PAUS system to image human lymphatic system in real-time. Results demonstrate that the system is able to image vascular and lymphatic vessels simultaneously. This could potentially provide detailed information regarding the interconnected roles of lymphatic and vascular systems in various diseases, therefore fostering the growth of therapeutic interventions.

ICG has a peak spectral absorption at approximately 810 nm and has almost no optical absorption above the wavelength of 900 nm. Exploiting this, a combination LED array with 820 and 940 nm that can toggle between these wavelengths at a rate of 4 kHz was developed. This study hypothesized that ICG administered into the lymphatic vessels will generate PA signal only when the LED array emits light of 820 nm wavelength. On the other hand, other tissue optical absorbers like melanin and blood vessels possess absorption characteristic in both 820 and 940 nm wavelengths, which in turn generates PA signals in both wavelengths. For differentiating veins from lymphatic vessels with ICG, the PA images generated at 940 nm can be divided by images at 820 nm. After acquiring and reconstructing PA data for both wavelengths, images are normalized for variations in optical energy. Then the 940 nm PA image is divided by the 820 nm image and displayed real-time (10 Hz) along with the pulse echo US image. Following the division of images, the jet colormap is used in such a way that image intensity values close to or above 1 (veins) are color coded in red and those pixels with values below 0.5 (ICG) are coded in blue. Apart from this, the systems' user interface also enables visualization of the images acquired with the two wavelengths separately along with the US image for real-time validation of the experimental procedures.

To perform real-time imaging of human lymphatic vessels and blood vessels in vivo, measurements on the limb of a healthy volunteer were made. Under the

guidance of a clinician, 0.1 ml of ICG (Diagnogreen 0.25%; Daiichi Sankyo Pharmaceutical, Tokyo, Japan) was injected subcutaneously into the first web space of the lower limb of a healthy person. ICG entering and flowing inside the lymph vessel was observed with a conventional fluorescent camera. After identifying the approximate position of a lymphatic vessel, real-time dual wavelength PAUS imaging was performed and the processed images were displayed (image generated by dividing 940 nm image with 820 nm image) along with conventional pulse echo US image.

Figure 15a and b shows PA images of 820 and 940 nm acquired at position 1 in which the probe was well aligned with a superficial vein. Beneath the melanin layer (marked with red arrow in 820 nm image), a superficial vein is clearly visualized in both PA images (double layered feature at a depth of ~2.3 cm, marked with pink arrow in 820 nm image). It is important to note that features visible in both the 820 and 940 nm images are identical at this position. Figure 15c and d show PA images of 820 and 940 nm acquired at position 2 in which the probe was aligned with a probable lymphatic vessel. At this position, common features evident in both wavelength images are likely to be veins (marked with pink arrows in 820 nm image). At a depth of ~2.6 cm, some bright features are visible only in the 820 nm image

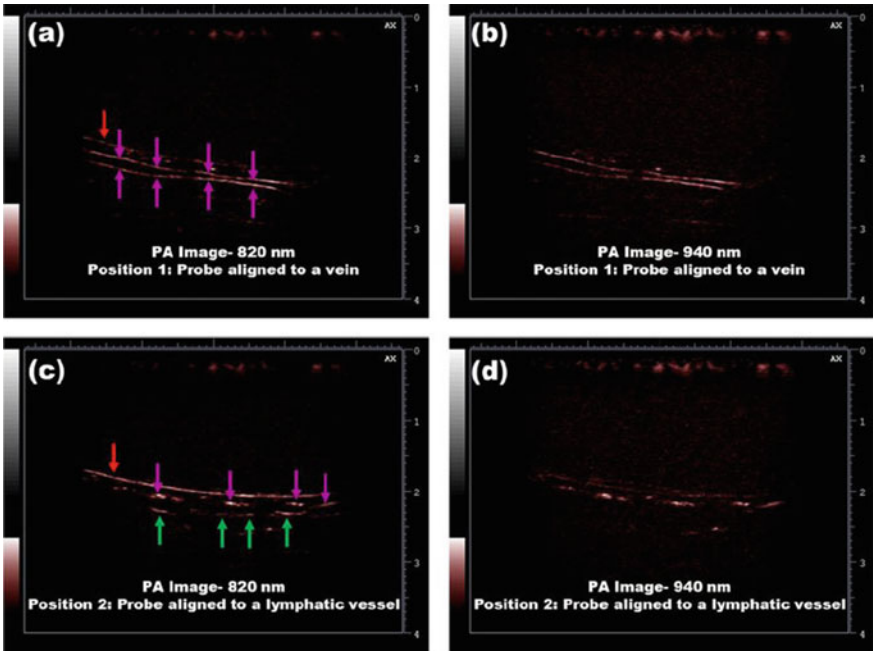

Fig. 15 **a** PA image—820 nm acquired when the probe was aligned to a superficial vein (position 1), **b** PA image—940 nm acquired when the probe was aligned to a superficial vein (position 1), **c** PA image—820 nm acquired when the probe was aligned to a lymphatic vessel (position 2), and **d** PA image—940 nm acquired when the probe was aligned to a lymphatic vessel (position 2). Red arrows—Melanin, Pink arrows—Veins, and Green arrows—Lymphatic vessel [Reprinted with permission from 45]

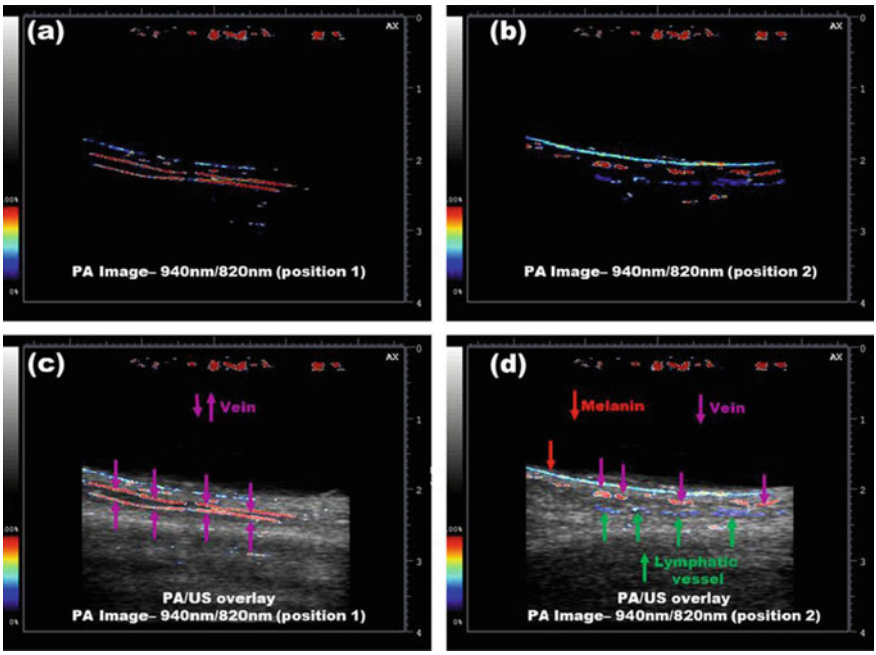

Fig. 16 **a** PA image—940/820 nm acquired when the probe was aligned to a superficial vein (position 1), **b** PA image—940/820 nm acquired when the probe was aligned to a lymphatic vessel (position 2), **c** 940/820 nm PA image overlaid on US image when the probe was aligned to a superficial vein (position 1), and **d** 940/820 nm PA image overlaid on US image when the probe was aligned to a lymphatic vessel (position 2). Red arrows—Melanin, Pink arrows—Veins, and Green arrows—Lymphatic vessel [Reprinted with permission from 45]

(Fig. 15c, marked with green arrows). These may be lymphatic vessels with ICG contrast.

Figure 16a shows the PA image obtained by dividing 940 and 820 nm images at position 1. As expected, the vein inside the imaging plane is visualized in red color since there is not much difference in absorption coefficient of venous blood in these two wavelengths. Figure 16b shows the PA image (940/820 nm) at position 2 where the probable lymphatic vessel is inside the imaging plane. In this case, we can see several features in blue color which confirms that these are lymphatic vessels. The ratio of 940 and 820 nm images resulted in low values in these areas since ICG inside lymphatic vessel is expected to absorb only 820 nm light. Figure 16c and d shows the same 940/820 nm PA images at two positions, but overlaid on conventional US images in gray scale.

From these results, it is evident that, by using a two-wavelength approach, we can simultaneously visualize and separate vein, lymphatic vessel, and melanin in vivo with high spatial and temporal resolution. It is worth mentioning that, these results were obtained at a frame rate of 10 Hz for two-wavelength PA imaging (along with processing for color-coded visualization) interleaved with pulse echo US imaging.

This is the first report on visualization of human lymphatic vessels using an LED-based PAUS system.

2.9 *Multispectral Photoacoustic Characterization Using LED-PAUS System*

The commercial LED-PAUS system has been so far used to perform either single or dual wavelength PA imaging. However, true advantages of photoacoustic imaging lies in being able to spatially un-mix multiple (more than two) tissue chromophores. This necessitates the use of more than two wavelengths. Towards this goal, this study from Shigeta [46] demonstrates the use of multiple wavelength LED arrays with the commercial LED-PAUS system. Here, the absorption spectra of ICG and porcine blood is photoacoustically measured using LED arrays with multiple wavelengths (405, 420, 470, 520, 620, 660, 690, 750, 810, 850, 925, 980 nm). Measurements were performed in a simple reflection mode configuration in which LED arrays where fixed on both sides of the linear array ultrasound probe. Phantom used consisted of micro-test tubes filled with ICG and porcine blood, which were placed in a tank filled with water, as shown in Fig. 17.

Figure 18a shows the PA signal intensities from ICG and hemoglobin with respect to different excitation wavelengths. Figure 18b shows PA intensities with respect to wavelengths normalized to optical output power of 660 nm LED arrays. It is evident that hemoglobin absorption is higher in lower wavelengths and ICG is highly absorbing in the range of 800–925 nm. For ICG, an absorption peak at the wavelength of 850 nm is visible. It is worth mentioning that the measured spectral behavior of

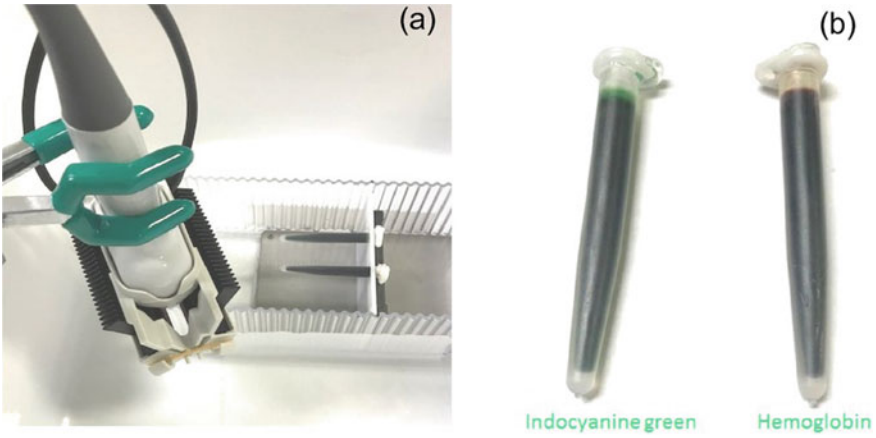

Fig. 17 **a** Experimental set up and, **b** photograph of micro-test tubes filled with ICG and porcine hemoglobin [Reprinted with permission from 46]

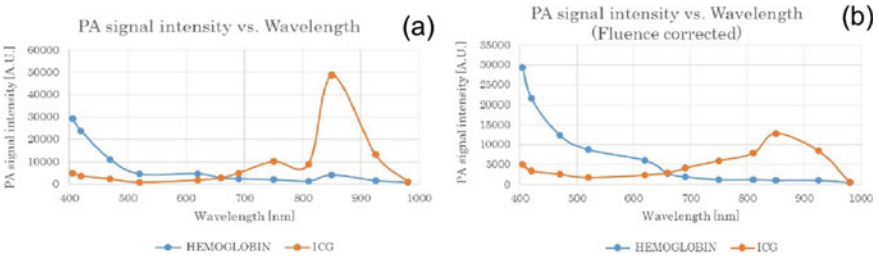

Fig. 18 **a** Measured PA signal intensities at different wavelengths, and **b** PA intensities with respect to wavelengths normalized to optical output power of 660 nm LED arrays [Reprinted with permission from 46]

ICG and hemoglobin (blood) is matching reasonably well with the reference values. These results demonstrate the potential capability of LED based PAUS system in performing clinical/pre-clinical multispectral photoacoustic imaging.

3 LED-Based PACT System

We recently developed a low-cost and portable PACT system [47, 48] using multi-wavelength LED arrays as optical sources and a linear ultrasound transducer array for the photoacoustic detection exploiting the commercial LED based B-mode PAUS system. In this section, we cover both the hardware implementation and the reconstruction of the LED-PACT system. We also present different validation studies comparing the capabilities of conventional LED-PAUS system with the LED based PACT system.

3.1 Design of LED-Based PACT System

A schematic of our experimental setup for the LED based photoacoustic computed tomography system is shown in Fig. 19d. A 3-D printed cylindrical tank, with an inner diameter of 38 mm, is used as the imaging cylinder. This imaging cylinder consists of five slots for housing the four LED arrays and one linear US probe. The cylinder with US probe and LEDs is attached to a rotational stage (PRMTZ8, ThorLabs Inc., Newton, NJ, USA). We have mounted this rotational stage in the inverted configuration as shown in Fig. 19d, f. The rotational axis of the stage is aligned with the vertical axes of the cylindrical imaging tank. The object to be imaged is embedded into a scattering phantom and this phantom is then attached to a phantom holder, as shown in Fig. 19d. The phantom is inserted into the imaging tank from the bottom (as shown in Fig. 19f) and is kept stationary during the rotational acquisition.

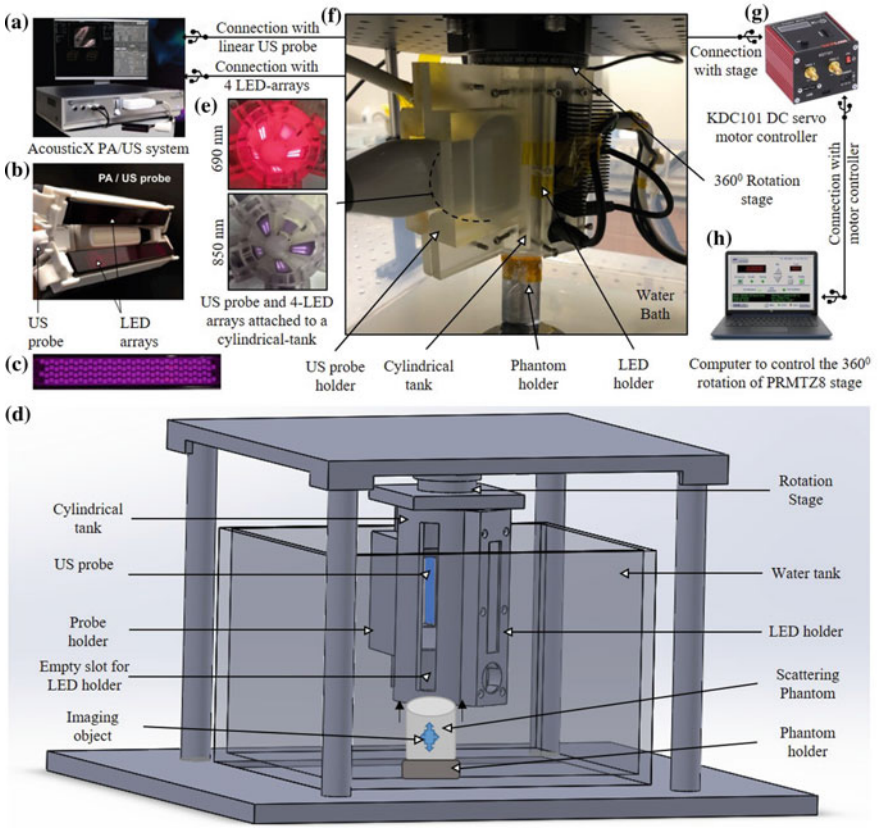

Fig. 19 Schematic representation of our LED based photoacoustic computed tomography (PAT) system. **a** Commercial LED-based combined photoacoustic/ultrasound (PA/US) system. **b** Typical arrangement of the two LED arrays and the US probe for B-mode PA/US imaging. **c** Optical image of an LED array consisting of four rows of 36 LEDs of dimension 1 mm × 1 mm. **d** Schematic showing the hardware implementation of our system consisting of a linear ultrasound probe and four LED arrays attached to an imaging cylinder mounted on rotation stage. Schematic also shows the placement of an imaging object. **e** Optical images showing the placement of four LED arrays (690/850 nm) and the US probe around a cylindrical tank of inner diameter 38 mm. **f** Photograph of our complete tomography setup with the LEDs, probe and the rotation stage controlled by the motor controller shown in (**g**). **h** Computer giving control signals to the controller for rotation of stage [Reprinted with permission from 47, 48]

Four LED holders (3-D printed, shown in Fig. 19d) housed in the cylindrical tank, hold the multi-wavelength LED arrays such that the stationary phantom is uniformly illuminated at all rotational positions. Figure 19e shows an example arrangement of four LED arrays (with each having 850/690 nm pair) and a linear US probe. The two sub-images in Fig. 19e shows the illumination at 690 and 850 nm wavelength achieved by selectively switching ON or OFF the respective wavelengths' LEDs from the LED array pairs, achieving uniform illumination at both the wavelengths.

The servo motor controller (KDC101 DC, ThorLabs Inc., Newton, NJ, USA, shown in Fig. 19g) controls the rotation stage with the help of a separate computer, shown in Fig. 19h. 2-D RF-Scan mode of commercial LED-PAUS system is used to acquire the B-mode PA images at all rotational positions and the acquired raw data is processed offline to reconstruct the volumetric 3-D photoacoustic computed tomography image at each wavelength.

While commercial B-mode LED-PAUS systems can only use two LED arrays at a time, the proposed LED-PACT system geometry is capable of employing more than four LED arrays used in this study. This not only increases the optical energy density inside the tissue medium, but also allows custom integration of multi-wavelength LEDs suitable for spectroscopic photoacoustic imaging.

3.2 LED-PACT Data Acquisition and Image Formation

The system acquires the PA data at a sampling rate of 40 MHz and the data is transferred to the graphical processing unit using USB 3.0 connection from the DAQ. One PA frame is acquired for each pulse of LED excitation. After the required PA frame averaging, the raw data is saved into the PC. During the 360° rotation, with a frame averaging of 2560 and pulse repetition frequency of 4 kHz, we have acquired a total of 90 frames, with 4° rotational steps. Total PA raw data corresponds to the 1024 time samples captured for each of the 128-transducer elements for each of these 90 frames, i.e. the size of the data matrix is $90 \times 1024 \times 128$.

A model-based time-reversal reconstruction algorithm [49] is applied, which numerically propagates the received photoacoustic pressure data back into the tissue medium from all the transducer elements. An Intel Xeon (2.1 GHz 32-core) based computer with 128 GB RAM and Nvidia Titan Xp GPU was used for the reconstruction. Since the computation time of model-based reconstruction methods increases exponentially with the size of the computational grid, two-dimensional computations can be orders of magnitude faster than three-dimensional computations. To be computationally efficient, we have applied the time-reversal algorithm in the 2-D plane formed by the rotation of a single transducer element. This is repeated for all 128-transducer elements individually, forming two-dimensional slices of the 3-D volume in 300 μm steps. The final 3-D image is formed by concatenating the 128 2-D slices into a single three-dimensional volume. With the above computational configuration, the total scan time for full tomography took around 102 s for each wavelength and about five minutes for the image reconstruction using the time-reversal algorithm.

3.3 Simulation and Experimental Studies

In this section, we first present a comparison study for the light fluence distribution along the imaging region in Sect. 3.3.1. Here, we have compared our proposed

strategy for LED arrays' placement along the cylindrical tank for performing the LED based PACT, with the conventional approach of using two LED arrays in LED-PAUS. This section also presents several validation studies to compare the capabilities of our LED based PACT system with the conventional LED based PAUS system.

3.3.1 Comparison Study for Fluence Distribution

There are two distinct ways of numerically calculating the optical fluence distribution in a system. The first and most accurate method is to use a Monte Carlo simulation for light transport [50, 51]. While Monte Carlo simulations are able to more precisely model the light transport, there can be an exceptional computational burden for large spatial grids, especially in three dimensions. An alternative to Monte Carlo methods, when working in the photoacoustic regime, is to model the diffusion approximation to the radiative transport equation [52]. The diffusion approximation uses a partial differential equation that is computationally much faster than similar Monte Carlo methods, with acceptable accuracy when used in the photoacoustic regime [52]. In order to measure the difference in fluence distribution between LEDs and laser, as well as different geometries of light source, we have applied the finite difference method in MATLAB to solve the optical diffusion equation [52–54]:

$$\nabla \cdot D(x)\nabla\Phi(x) + \mu_a(x)\,\Phi(x) = 0,\ x \in X; \quad \Phi(y) = q(y),\ y \in \partial X \tag{1}$$

In this equation, $D = [3(\mu_a + \mu_s')]^{-1}$ is the diffusion coefficient, where $\mu_a = 0.1\ \mathrm{cm}^{-1}$ and $\mu_s' = 10.0\ \mathrm{cm}^{-1}$ are the absorption and reduced scattering coefficients of the simulated tissue medium. q(y) represents the optical source located at the boundary, either the LEDs or laser surrounding the region of interest.

As described in Sect. 2, the LED arrays used in this study consists of 1 mm x 1 mm LEDs arranged in a 2-D matrix form (4 rows and 36 columns). For a dual wavelength LED array (e.g. 850/690 nm), alternate two of the four rows are of same wavelength. Each of the element present in the array is separated by a 1 mm distance in all directions from the neighbor elements. We have defined these LED arrays in a three dimensional grid and have calculated the fluence distribution for a typical homogeneous tissue medium to study the effect of placing these arrays in the proposed approach.

Figure 20 presents a detailed study of the fluence distribution comparing our proposed approach (LED-PACT) with the conventional approach of placing the LED arrays for performing LED based PAUS imaging. Figure 20a shows an X–Y plane map with two LED arrays (shown in white, each array's two elements are shown corresponding to the 850 nm wavelength) placed at the left and right side of an ultrasound transducer (shown in blue) along the imaging circle (X–Y plane of the cylindrical imaging tank) shown in orange. Figure 20b shows a similar X–Y plane map with four LED arrays as proposed, placed along the orange circle and separated by 72° from each LED array and the ultrasound transducer (shown in blue). Figure 20c, d show the three-dimensional arrangement of the LED arrays along the cylindrical imaging

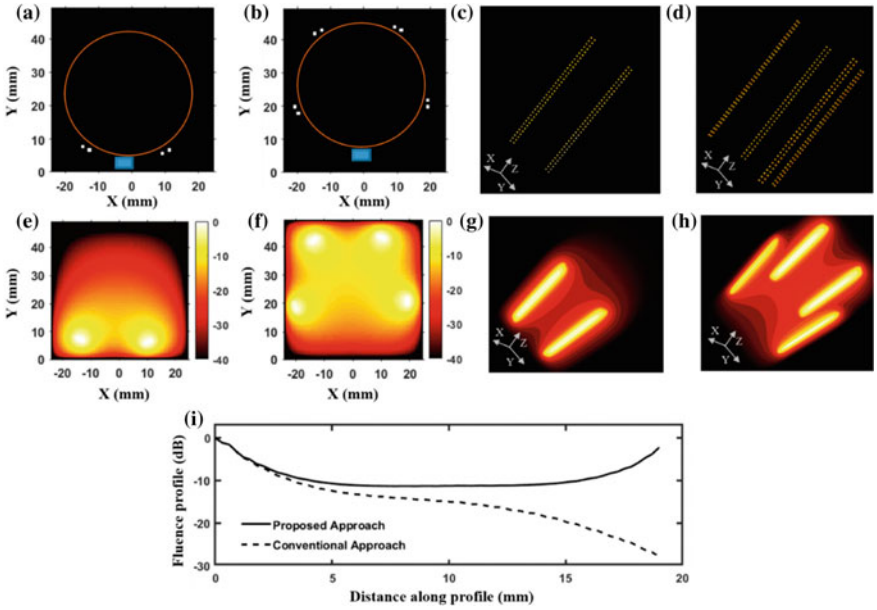

Fig. 20 Comparison of optical fluence distribution inside the tissue medium of 5 cm diameter for the proposed LED-based PACT and the conventional B-mode PAUS systems. **a** Schematic of LED-PAUS geometry consisting of two 850/690 nm LED arrays (white dots) and a linear ultrasound transducer array (blue rectangle) placed on the boundary (orange circle) of the tissue medium. **b** Similar schematic for the PACT geometry shows the arrangement four LED arrays with 72° separation and the ultrasound transducer. **c**, **d** show the corresponding 3-D schematic positions of the LED arrays in the PAUS and our PACT systems. Individual dots represent the positions of LED elements for a given wavelength in the dual-wavelength LED array. **e**, **f** show the 2-D optical fluence map inside the tissue medium for the two schematics shown in (**a**) and (**b**) respectively. **g**, **h** show the 3-D fluence distribution for the two schematics shown in (**c**) and (**d**) respectively. **i** Shows the fluence profile comparison along a diagonal in the imaging circles of the PAUS geometry shown in (**a**) and the PACT illumination shown in (**b**) [Reprinted with permission from 47]

tank for the conventional and the proposed approach, respectively. The X–Y cross-sections of the simulated fluence maps with the conventional and proposed approach are shown in Fig. 20e, f and the corresponding three dimension fluence are shown in Fig. 20g, h.

To study the changes in the fluence across the width of the imaging tank, we have plotted the magnitude (in dB) of the fluence in an X–Y plane (at the middle of the cylindrical tank) along the diagonal. Figure 20i shows the fluence profile plot for the conventional and the proposed approach clearly presenting the advantages of using the four LED arrays along the imaging tank.

3.3.2 Structural Imaging Studies

To compare the structural imaging capabilities of our developed PACT system with the commercial LED-PAUS system, we have imaged four pencil lead targets structurally placed in the imaging region. The four targets are embedded in to 1.5% agarose phantom cylinder with diameter of 35 mm, height of 80 mm.

To mimic the tissue scattering, intralipid (INTRALIPID 20% IV Fat Emulsion, VWR international, Radnor, PA, USA) was added to the agarose phantom to achieve reduced scattering coefficient of 10 cm^{-1}. Figure 21a–c shows the schematic side view, side view photograph and top view photograph of the phantom respectively. In this phantom, we have three 0.3 mm diameter pencil leads (marked as 2, 3 and 4 in Fig. 21a), and one bundle (group of 5 0.3 mm diameter pencil leads with total diameter of ~0.9 mm) marked as 1 in Fig. 21a.

To compare these results with the conventional B-mode LED-PAUS system 3-D scan, we have scanned the phantom in Fig. 21a using two LED arrays (850 nm) and the same ultrasound probe, with the arrangement shown in Fig. 19b. The 3-D

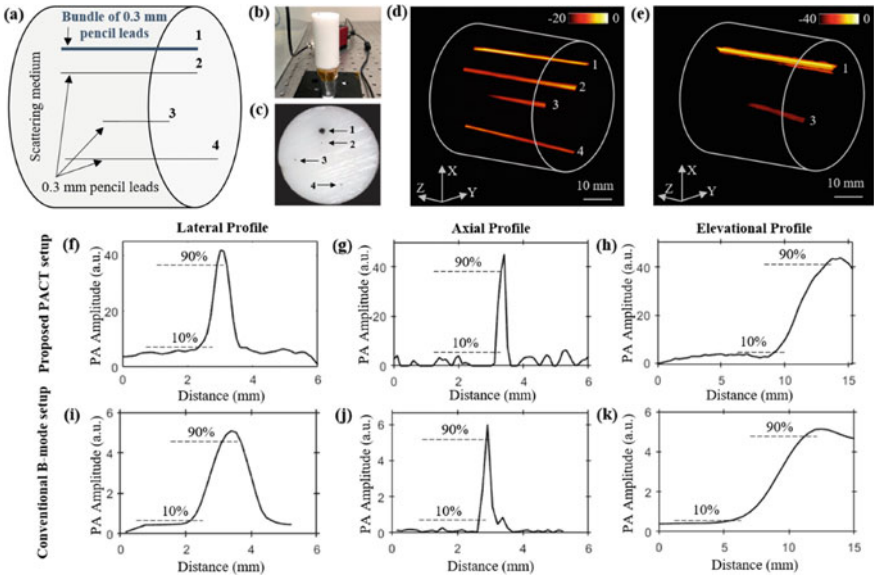

Fig. 21 Comparing the structural imaging capabilities of the LED-based PACT and PAUS systems using a pencil lead phantom. **a** Schematic showing side view of a tissue-mimicking intralipid phantom with four targets embedded. The depth of targets from the top surface of the phantom are as follows: 1 (bundle of five 0.3 mm pencil leads: at 10 mm), 2 (0.3 mm pencil lead: at 14 mm), 3 (0.3 mm pencil lead: at 23 mm), 4 (0.3 mm pencil lead: at 31 mm). **b**, **c** Photographs of the side and top views of the phantom. Reconstructed 3-D volume rendered photoacoustic image (**d**) using PACT, and **e** linear scanning of the conventional PAUS systems. Photoacoustic amplitude plots of the pencil lead target #3, located at 23 mm depth inside the medium, along the lateral, axial and elevational directions of the volume rendered (**f–h**) PACT image shown in (**d**) and **i–k** the linear scan image shown in (**e**) [Reprinted with permission from 47]

reconstructed volume rendered PA image for conventional b-mode 3-D scan is shown in Fig. 21e. Only the pencil lead "3", and the bundle "1" was seen in the reconstructed image. This is due to the following two limitations of using conventional B-mode LED-PAUS system. (1) With a lower LED light source, a small photoacoustic target located behind/below a thick/big photoacoustic target, is likely to be shadowed in conventional B-mode imaging. The same target when imaged with our proposed LED based PACT system, is detected with a decent SNR. (pencil lead "2" shown in Fig. 21). (2) While using conventional LED-PAUS system [24–29], the angular arrangement of LED arrays around the ultrasound probe as shown in Fig. 1, leaves about 8–10 mm of standoff region. The pencil lead "4" is about 31 mm from the top surface of the phantom. Hence, with the 8–10 mm of standoff, the conventional B-mode LED-PAUS system having a maximum data acquisition capability of 38 mm, fails to detect this target. However, due to negligible standoff with our PACT configuration, the same pencil lead target "4" is detected with a decent SNR.

We further studied the spatial resolution of our proposed LED based PACT system using the broken pencil lead "3" shown in Fig. 21a. A comparison study for LED-PACT versus LED-PAUS system is performed by calculating the lateral, axial and elevational resolutions with the plots shown in Fig. 21f–k. Peak photoacoustic amplitude for the pencil lead target "3" was plotted with respect to the lateral, axial and elevational distance as shown in Fig. 21f–h and i–k respectively for PACT and PAUS scans. The profiles shown in the plots were used to estimate the resolution of the system. Half of the distance between 90 and 10% of the peak photoacoustic amplitude was calculated as 300 μm in the lateral direction for PACT system as shown in Fig. 21f. Lateral resolution for PAUS system was calculated as 600 μm as shown in Fig. 21i. Similarly, the axial, elevational resolutions of PACT system and PAUS system were calculated as 120 μm, 2.1 mm and 130 μm, 3 mm respectively.

These experiments demonstrated that the PACT system can see through the shadow (blind spot) imaging regions of the conventional PAUS systems and visualize smaller targets hiding behind larger targets. These experiments also demonstrated that the spatial resolutions of the PACT system are better than the PAUS. These advantages can be attributed to the fact that the PACT system enables more uniform illumination of the imaging region during the 360° rotation. The conventional LED-PAUS systems require the imaging head to be 10 mm above the tissue surface to achieve uniform illumination of the phantom. This 10 mm standoff is usually filled with ultrasound coupling medium and leads to several complications such as (1) creation of bubbles and associated artifacts during the linear scan, (2) ultrasound and optical attenuation inside the thick coupling medium, (3) uncomfortable imaging of living subjects, and (4) extended imaging depth and computer memory which reduces imaging speed. The LED-PACT system demonstrated here required no such stand-off and therefore could image all 4 pencil lead targets inside the phantom, whereas the LED-PAUS system misses the target-4 at 31 mm depth.

3.3.3 Dual-Wavelength Imaging with Our PACT System

In this section, we have presented the capabilities of our system to perform dual wavelength photoacoustic computed tomography. To perform dual-wavelength imaging, we have employed the 850/690 nm LED array pairs. Each of the four LED arrays placed around the cylinder tank can be toggled to provide either 850 or 690 nm light, as shown in Fig. 19e. At each rotation step of 4°, two different frames are acquired corresponding to the two wavelengths of LEDs used. We have validated our approach by imaging two phantoms, with one having only endogenous photoacoustic targets (blood and melanin) and the other having a combination of blood with an exogenous contrast, i.e. Indocyanine-green (ICG).

Figure 22a shows the geometry of our first phantom. Here, highly oxygenated blood (Bovine Blood CITR, Carolina Biological Supply, Charlotte, NC, USA) and 0.1 mM Melanin solution (M8631, Sigma-Aldrich, St. Louis, MO, USA) were filled separately in 0.5 mm outer diameter tubes. These tubes were embedded in to 1.5% agarose phantom cylinder with diameter of 35 mm, height of 80 mm. To mimic the tissue scattering, intralipid (INTRALIPID 20% IV Fat Emulsion, VWR international, Radnor, PA, USA) was added to the agarose phantom to achieve reduced scattering

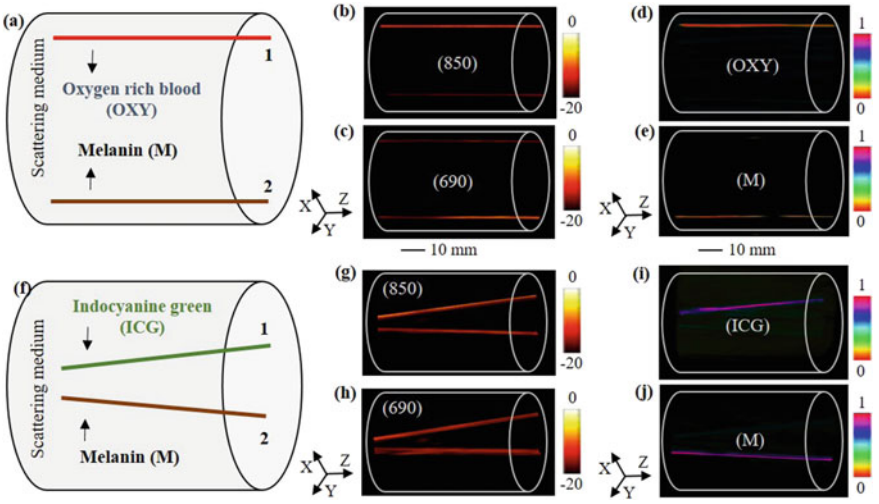

Fig. 22 Dual-wavelength imaging with LED based photoacoustic computed tomography system: validation over two phantoms. **a** First phantom: showing geometrical placement of the Oxygen rich blood (OXY) tube and a Melanin (M) tube inside scattering phantom. **b**, **c** 3-D PACT images of the phantom with 850 and 690 nm LED light illumination respectively. **d**, **e** Spectrally unmixed 3-D volumetric images of the phantom using the results in (**b**, **c**) highlighting the spatial distribution of (OXY) and (M) tubes respectively. **f** Second phantom: showing geometrical placement of the ICG tube and a Melanin (M) tube inside scattering phantom. **g**, **h** 3-D PACT images of the phantom at 850 nm and 690 nm illumination respectively. **i**, **j** Spectrally unmixed 3-D volumetric images of the phantom highlighting the spatial distribution of (ICG) and (M) tubes respectively [Reprinted with permission from 48]

coefficient of 10 cm^{-1}. Figure 22b, c shows the reconstructed volumetric 3-D PACT images for the above phantom with the 850 nm and 690 nm wavelengths respectively. With the dual wavelength tomography data acquired with our setup, we also applied a linear unmixing technique to separate the two types of chromophores imaged, viz. oxy rich blood and melanin. As the absorption of these chromophores differs significantly at the above two wavelengths, we could separate them spatially, as shown in Fig. 22d, e.

In our second study, we arranged ICG (with 1250 μM concentration) and Melanin (1 mM concentration) tubes inside similar scattering medium. Figure 22f shows the geometry of our second phantom. Figure 22g, h shows the reconstructed volumetric 3-D PACT images for our second phantom with the 850 nm and 690 nm wavelengths respectively. We further applied linear unmixing technique to separate these two chromophores, viz. ICG and melanin, and were able to separate them spatially, as shown in Fig. 22i, j.

3.3.4 Oxygen Saturation with Our PACT System

We further validated the vascular oxygen saturation imaging capabilities of the LED-PACT system by imaging a human finger mimicking phantom using four dual-wavelength 850/690 nm LED arrays. The human finger anatomy can be understood with the help of the schematic shown in Fig. 23a. For mimicking the finger, we used a high scattering intralipid phantom (reduced scattering coefficient of 15 cm^{-1}) and embedded an animal bone inside it. We further embedded the two types of blood tubes (Bovine Blood CITR, Carolina Biological Supply, Charlotte, NC, USA), namely, high-oxygenated (oxy-rich) tube and the low-oxygenated (oxy-poor) tube, both with outer diameter of 0.5 mm. The side view and top view optical images of the phantom are shown in Fig. 23b, c respectively.

The experimental setup used to image this phantom consisted of four 850/690 nm LED array pairs. Each of the four LED arrays placed around the cylinder tank can be toggled to provide either 850 or 690 nm light, as shown in Fig. 19e. At each rotation step of 4°, two different frames are acquired corresponding to the two wavelengths of LEDs used. Figure 23d–f represents the ultrasound, photoacoustic (at 850 nm) and co-registered (US + PA) frames at a single rotation step, captured during the full tomography acquisition. The structure of the finger is visible in the US frame whereas the presence of blood tubes can be seen using PA frame. With our proposed approach, the full 3-D volume rendered PACT images generated for the above phantom are shown in Fig. 23g, h, with 850 nm and 650 nm LED illumination respectively. Figure 23i shows the volumetric oxygen saturation map of the finger phantom obtained using the PACT images at the mentioned two wavelengths.

The LED-PACT configuration delivered higher (400 μJ) pulse energy for each 850 nm as well as 690 nm wavelengths than possible with the conventional LED-PAUS systems that can accommodate only two such LED arrays. This enabled mapping of vascular oxygen saturation from deeper regions.

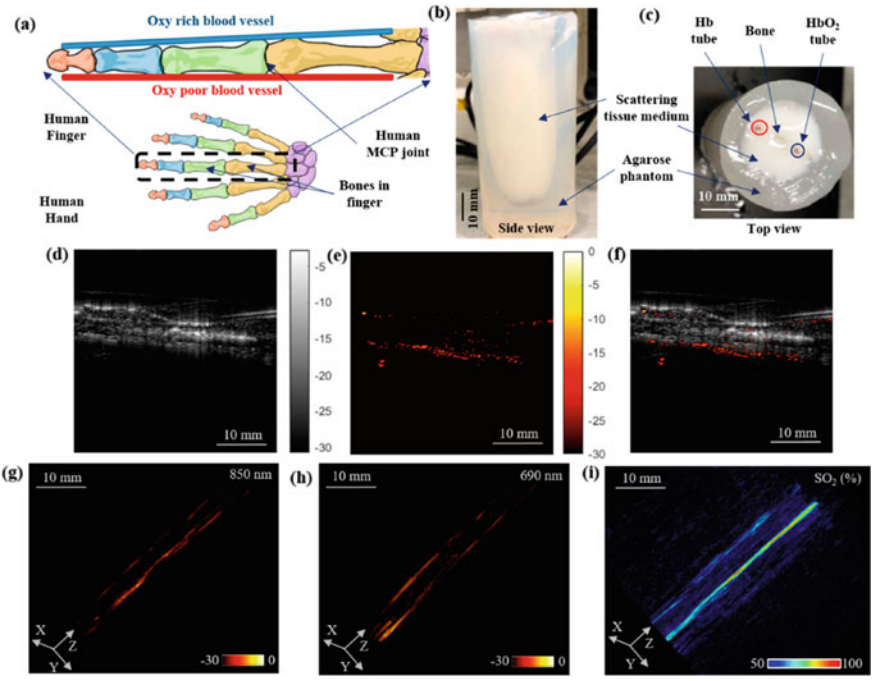

Fig. 23 LED-PACT-imaging of vascular oxygen saturation using a human finger-mimicking phantom. **a** Schematic sketch of a typical human finger with the location of bones and the blood vessels (oxy rich: HbO_2; and oxy poor: Hb). **b**, **c** Show the side and the top view photographs of the finger phantom consisting of bone and blood vessels. **d** The ultrasound (US), **e** photoacoustic (PA), and **f** co-registered US + PA frames acquired at one of the rotational steps during the 360° rotation around the phantom. **g**, **h** The reconstructed 3-D volume rendered PACT images of the finger phantom using 850 nm and 690 nm LED illuminations respectively. **i** Shows the spectrally unmixed volumetric oxygen saturation map for the finger phantom [Reprinted with permission from 47]

3.3.5 Multi-spectral Imaging with Our PACT System

One of the main advantages of our LED-PACT system, compared to the existing LED-based PAUS system, is that it can be easily adapted to allow custom designed multi-wavelength excitation using multiple LED arrays, to enable similar functional and molecular imaging capabilities of tunable lasers. This is demonstrated by imaging a tissue mimicking phantom embedded with three chromophores having different optical absorption spectra using two dual-wavelength 850/690 nm LED arrays and two 470 nm LED arrays. Each of these four LED arrays placed around the cylinder tank can be selectively switched "ON" or "OFF" to provide either 850, 690 or 470 nm light. At each rotation step of 4°, three different frames are acquired corresponding to the three wavelengths of LEDs used. In this study, we have imaged three biologically relevant chromophores, i.e. Indocyanine-green (ICG), Methylene blue (MB) and melanin, embedded in a high scattering phantom.

Figure 24a shows the geometry of our phantom. Here, 1 mM Melanin solution, 1 mM ICG solution and 1 mM MB solution were filled separately in 0.5 mm outer diameter tubes. These tubes were embedded in to 1.5% agarose phantom cylinder with diameter of 35 mm, height of 80 mm. To mimic the tissue scattering, intralipid (INTRALIPID 20% IV Fat Emulsion, VWR international, Radnor, PA, USA) was added to the agarose phantom to achieve reduced scattering coefficient of 10 cm^{-1}. Figure 24b shows the optical top view image of the phantom. Figure 24c–e shows the arrangement of US probe and the four LED arrays used for illuminating the phantom with 850 nm, 690 nm, and 470 nm light respectively. To maintain uniform distribution of light for the three wavelengths, out of the two 850/690 nm LED arrays, one is placed close to the transducer and the other one is placed at diagonally opposite

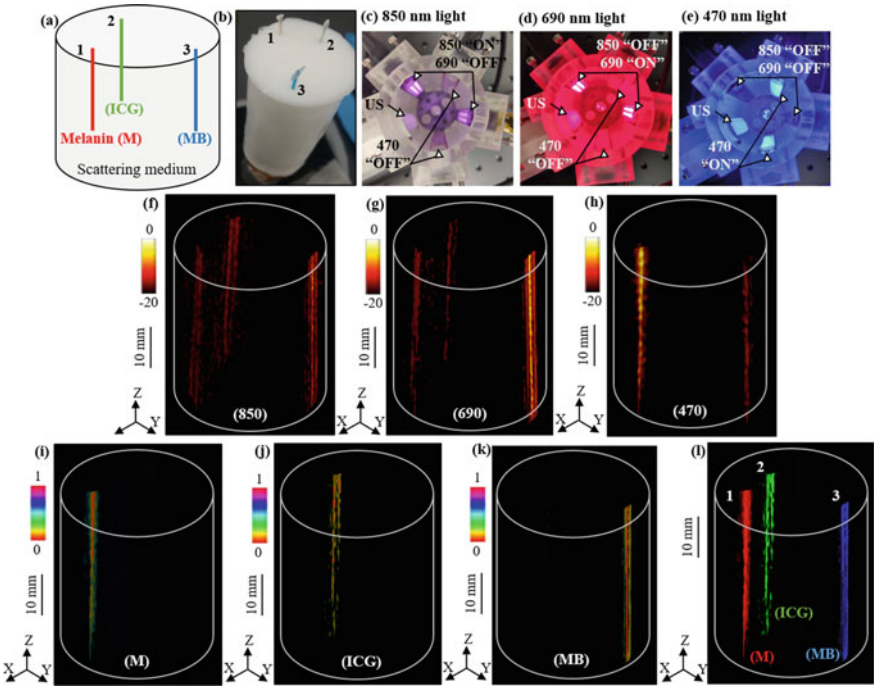

Fig. 24 LED based multispectral photoacoustic computed tomography. **a** Schematic view and **b** a photograph of the tissue mimicking cylindrical phantom of 35 mm diameter and 80 mm height. The phantom is embedded with 0.5 mm polyethylene tubes filled with 1 mM concertation solutions of melanin (M), indocyanine-green (ICG), and methylene blue (MB) **c–e** Show the arrangement of ultrasound (US) transducer array, two 850/690 nm LED arrays and two 470 nm LED arrays with sequentially switched 850 nm, 690 nm and 470 nm wavelength emissions from the arrays. **f–h** 3-D PACT images of the phantom acquired with 850 nm, 690 nm and 470 nm illumination respectively. **i–k** Spectrally unmixed volumetric images of the phantom, obtained from the multispectral PA images in (**f–h**), show the spatial distribution of M, ICG, and MB tubes respectively. **l** Superimposed 3-D unmixed image of the three chromophores. Scale bar is 10 mm in the images (**f–l**) [Reprinted with permission from 47]

corner. Similarly, one 470 nm LED array is placed closed to the transducer and the other one is placed at diagonally opposite corner. Figure 24c shows the configuration where we only switch ON the 850 nm light from the 850/690 nm pairs. The total output energy in this case is 200 μJ. Similarly, in Fig. 24d, we switch ON the 690 nm light from the 850/690 pairs giving the same output energy of 200 μJ. To maintain the same energy and distribution for 470 nm light, we switch ON only half of the LEDs in each of the 470 nm arrays as shown in Fig. 24e.

Figure 24f–h shows the reconstructed volumetric PAT images for the above phantom with the 850 nm, 690 nm, and 470 nm wavelengths respectively. Since the optical absorption of melanin decreases with increase in the optical wavelength, the PA contrast of the melanin is higher at 470 nm and lower in the 870 nm PACT images. Similarly, the peak absorption of MB ~680 nm correlates well with the highest PA intensity of the MB tube at the 690 nm wavelength. With the three wavelengths tomography data acquired with our setup, we also applied a linear unmixing technique to separate the three types of chromophores imaged, viz. Melanin, ICG, and MB. Based on these spectral trends, the linear spectral unmixing technique could easily separate the three chromophores, as shown in Fig. 24i–k. We further superimposed the three unmixed images to visualize and confirm the respective spatial distribution of the three chromophores in the given 3-D volume, as shown in Fig. 24l.

This current study is designed to demonstrate the above described various advantages of our novel LED-PACT system using proof-of-concept experiments on tissue mimicking phantoms. The imaging performance of the LED-PACT system can be further improved from multiple directions. This includes a better imaging geometry that employs more than 4 LED arrays, faster data acquisition, model-based image reconstruction algorithms [55–57] and deep learning approaches [58–60]. Fully developed LED-PACT will can be validated on living subjects such as imaging small animals and human body parts such as finger, wrist and breast.

4 Conclusion

In this chapter, we first discussed the commercial LED-based dual mode Photoacoustic and Ultrasound imaging system, referred to as LED-PAUS system. We have presented several phantom as well as in vivo studies demonstrating the capabilities as well as limitations of the commercial LED-PAUS system. This chapter also presents our recently developed LED based photoacoustic computed tomography system, referred to as LED-PACT system that integrates four LED arrays and a linear ultrasound transducer array in a cylindrical housing. The LED-PACT system has several benefits compared to the existing LED-based PAUS systems, such as multispectral photoacoustic imaging, better spatial resolution, uniform illumination, and improved imaging depth. Validation experiments on different tissue mimicking phantoms demonstrated the structural, functional and molecular photoacoustic imaging capabilities of the system. With further optimization, such as increase in

the number of LED arrays and model-based image reconstruction, LED based PACT imaging systems herald a promising biomedical imaging tool of living subjects.

Acknowledgements LED-PACT project was partially funded by the NIH-NIBIB R00EB017729-04 (SRK) and Penn State Cancer Institute (SRK). We also acknowledge the support of NVIDIA Corporation with the donation of the Titan X Pascal GPU used for the reconstruction of LED-PACT images. We further thank CYBERDYNE Inc. for their technical support.

References

1. P. Beard, Biomedical photoacoustic imaging. Interface Focus **1**, 602–631 (2011)
2. X. Wang, Y. Pang, G. Ku, X. Xie, G. Stoica, L.V. Wang, Noninvasive laser-induced photoacoustic tomography for structural and functional in vivo imaging of the brain. Nat. Biotechnol. **21**, 803 (2003)
3. L. Lin, P. Hu, J. Shi, C.M. Appleton, K. Maslov, L. Li, R. Zhang, L.V. Wang, Single-breath-hold photoacoustic computed tomography of the breast. Nat. Commun. **9**, 2352 (2018)
4. R.A. Kruger, C.M. Kuzmiak, R.B. Lam, D.R. Reinecke, S.P. Del Rio, D. Steed, Dedicated 3D photoacoustic breast imaging. Med. Phys. **40**, 113301 (2013)
5. L. Li, L. Zhu, C. Ma, L. Lin, J. Yao, L. Wang, K. Maslov, R. Zhang, W. Chen, J. Shi et al., Single-impulse panoramic photoacoustic computed tomography of small-animal whole-body dynamics at high spatiotemporal resolution. Nat. Biomed. Eng. **1**, 0071 (2017)
6. H.P.F. Brecht, R. Su, M.P. Fronheiser, S.A. Ermilov, A. Conjusteau, A.A. Oraevsky, Whole-body three-dimensional optoacoustic tomography system for small animals. J. Biomed. Opt. **14**, 064007 (2009)
7. R. Ma, A. Taruttis, V. Ntziachristos, D. Razansky, Multispectral optoacoustic tomography (MSOT) scanner for whole-body small animal imaging. Opt. Express **17**, 21414–21426 (2009)
8. H. Chen, S. Agrawal, A. Dangi, C. Wible, M. Osman, L. Abune, H. Jia, R. Rossi, Y. Wang, S.R. Kothapalli, Optical-resolution photoacoustic microscopy using transparent ultrasound transducer. Sensors **19**(24), 5470 (2019)
9. K. Maslov, H.F. Zhang, S. Hu, L.V. Wang, Optical-resolution photoacoustic microscopy for in vivo imaging of single capillaries. Opt. Lett. **33**, 929–931 (2008)
10. T.T. Wong, R. Zhang, C. Zhang, H.C. Hsu, K.I. Maslov, L. Wang, J. Shi, R. Chen, K.K. Shung, Q. Zhou et al., Label-free automated three-dimensional imaging of whole organs by microtomy-assisted photoacoustic microscopy. Nat. Commun. **8**, 1386 (2017)
11. L. Xi, H. Jiang, High resolution three-dimensional photoacoustic imaging of human finger joints in vivo. Appl. Phys. Lett. **107**, 063701 (2015)
12. K. Fukutani, Y. Someda, M. Taku, Y. Asao, S. Kobayashi, T. Yagi, M. Yamakawa, T. Shiina, T. Sugie, M. Toi, Characterization of photoacoustic tomography system with dual illumination, in *Photons Plus Ultrasound: Imaging and Sensing 2011*, vol. 7899 (International Society for Optics and Photonics, 2011), p. 78992J
13. X. Wang, D.L. Chamberland, D.A. Jamadar, Noninvasive photoacoustic tomography of human peripheral joints toward diagnosis of inflammatory arthritis. Opt. Lett. **32**, 3002–3004 (2007)
14. P. van Es, S.K. Biswas, H.J.B. Moens, W. Steenbergen, S. Manohar, Initial results of finger imaging using photoacoustic computed tomography. J Biomed Opt **19**, 060501 (2014)
15. Z. Deng, C. Li, Noninvasively measuring oxygen saturation of human finger-joint vessels by multi-transducer functional photoacoustic tomography. J Biomed Opt **21**, 061009 (2016)
16. M. Zafar, K. Kratkiewicz, R. Manwar, M. Avanaki, Development of low-cost fast photoacoustic computed tomography: system characterization and phantom study. Appl Sci **9**, 374 (2019)
17. A. Dangi, S. Agrawal, J. Lieberknecht, J. Zhang, S.R. Kothapalli, Ring Ultrasound transducer based miniaturized photoacoustic imaging system. IEEE, 1–4 (2018 IEEE SENSORS, 2018)

18. A. Dangi, S. Agrawal, S. Tiwari, S. Jadhav, C. Cheng, G.R. Datta, S. Trolier-McKinstry, R. Pratap, S.R. Kothapalli, Ring PMUT array based miniaturized photoacoustic endoscopy device, in *Photons Plus Ultrasound: Imaging and Sensing*, vol. 10878 (International Society for Optics and Photonics, February 2019), p. 1087811
19. J. Zhang, S. Agrawal, A. Dangi, N. Frings, S.R. Kothapalli, Computer assisted photoacoustic imaging guided device for safer percutaneous needle operations, in *Photons Plus Ultrasound: Imaging and Sensing*, vol. 10878 (International Society for Optics and Photonics, Feb 2019), p. 1087866
20. A. Dangi, S. Agrawal, G.R. Datta, V. Srinivasan, S.R. Kothapalli, Towards a low-cost and portable photoacoustic microscope for point-of-care and wearable applications. IEEE Sens. J. (2019)
21. K. Daoudi, P. Van Den Berg, O. Rabot, A. Kohl, S. Tisserand, P. Brands, W. Steenbergen, Handheld probe integrating laser diode and ultrasound transducer array for ultrasound/photoacoustic dual modality imaging. Opt. Express **22**, 26365–26374 (2014)
22. H. Zhong, T. Duan, H. Lan, M. Zhou, F. Gao, Review of low-cost photoacoustic sensing and imaging based on laser diode and light-emitting diode. Sensors **18**, 2264 (2018)
23. T.J. Allen, P.C. Beard, High power visible light emitting diodes as pulsed excitation sources for biomedical photoacoustics. Biomed. Opt. Express **7**, 1260–1270 (2016)
24. A. Hariri, J. Lemaster, J. Wang, A.S. Jeevarathinam, D.L. Chao, J.V. Jokerst, The characterization of an economic and portable LED-based photoacoustic imaging system to facilitate molecular imaging. Photoacoustics **9**, 10–20 (2018)
25. Y. Zhu, G. Xu, J. Yuan, J. Jo, G. Gandikota, H. Demirci, T. Agano, N. Sato, Y. Shigeta, X. Wang, Light emitting diodes based photoacoustic imaging and potential clinical applications. Sci. Rep. **8**, 9885 (2018)
26. W. Xia, M. Kuniyil Ajith Singh, E. Maneas, N. Sato, Y. Shigeta, T. Agano, S. Ourselin, S.J. West, A.E. Desjardins, Handheld real-time LED-based photoacoustic and ultrasound imaging system for accurate visualization of clinical metal needles and superficial vasculature to guide minimally invasive procedures. Sensors **18**, 1394 (2018)
27. T. Agano, N. Sato, H. Nakatsuka, K. Kitagawa, T. Hanaoka, K. Morisono, Y. Shigeta, Attempts to increase penetration of photoacoustic system using LED array light source, in *Photons Plus Ultrasound: Imaging and Sensing 2015*, vol. 9323 (International Society for Optics and Photonics, 2015), p. 93233Z.
28. Y. Adachi, T. Hoshimiya, Photoacoustic imaging with multiple-wavelength light-emitting diodes. Jp. J. Appl. Phys. **52**, 07HB06 (2013)
29. J. Jo, G. Xu, Y. Zhu, M. Burton, J. Sarazin, E. Schiopu, G. Gandikota, X. Wang, Detecting joint inflammation by an LED-based photoacoustic imaging system: a feasibility study. J. Biomed. Opt. **23**, 110501 (2018)
30. G.P. Luke, D. Yeager, S.Y. Emelianov, Biomedical applications of photoacoustic imaging with exogenous contrast agents. Ann. Biomed. Eng. **40**, 422–437 (2012)
31. S.R. Kothapalli, G.A. Sonn, J.W. Choe, A. Nikoozadeh, A. Bhuyan, K.K. Park, P. Cristman, R. Fan, A. Moini, B.C. Lee, J. Wu, T.E. Carver, D. Trivedi, L. Shiiba, I. Steinberg, D.M. Huland, M.F. Rasmussen, J.C. Liao, J.D. Brooks, P.T. Khuri-Yakub, S.S. Gambhir, Simultaneous transrectal ultrasound and photoacoustic human prostate imaging. Sci. Transl. Med. **11**, eaav2169 (2019)
32. M. Jeon, W. Song, E. Huynh, J. Kim, J. Kim, B.L. Helfield, B.Y. Leung, D.E. Geortz, G. Zheng, J. Oh et al., Methylene blue microbubbles as a model dual-modality contrast agent for ultrasound and activatable photoacoustic imaging. J. Biomed. Opt. **19**, 016005 (2014)
33. J. Wang, C.Y. Lin, C. Moore, A. Jhunjhunwala, J.V. Jokerst, Switchable photoacoustic intensity of methylene blue via sodium dodecyl sulfate micellization. Langmuir **34**, 359–365 (2017)
34. K. Cheng, S.R. Kothapalli, H. Liu, A.L. Koh, J.V. Jokerst, H. Jiang, M. Yang, J. Li, J. Levi, J.C. Wu et al., Construction and validation of nano gold tripods for molecular imaging of living subjects. J. Am. Chem. Soc. **136**, 3560–3571 (2014)
35. A. Dragulescu-Andrasi, S.R. Kothapalli, G.A. Tikhomirov, J. Rao, S.S. Gambhir, Activatable oligomerizable imaging agents for photoacoustic imaging of furin-like activity in living subjects. J. Am. Chem. Soc. **135**, 11015–11022 (2013)

36. M.T. Berninger, P. Mohajerani, M. Wildgruber, N. Beziere, M.A. Kimm, X. Ma, B. Haller, M.J. Fleming, S. Vogt, M. Anton et al., Detection of intramyocardially injected DiR-labeled mesenchymal stem cells by optical and optoacoustic tomography. Photoacoustics 6, 37–47 (2017)
37. J.V. Jokerst, M. Thangaraj, P.J. Kempen, R. Sinclair, S.S. Gambhir, Photoacoustic imaging of mesenchymal stem cells in living mice via silica-coated gold nanorods. ACS Nano **6**, 5920–5930 (2012)
38. S.Y. Nam, L.M. Ricles, L.J. Suggs, S.Y. Emelianov, In vivo ultrasound and photoacoustic monitoring of mesenchymal stem cells labeled with gold nanotracers. PLoS ONE **7**, e37267 (2012)
39. B. Zhang, X. Sun, H. Mei, Y. Wang, Z. Liao, J. Chen, Q. Zhang, Y. Hu, Z. Pang, X. Jiang, LDLR-mediated peptide-22-conjugated nanoparticles for dual-targeting therapy of brain glioma. Biomaterials **34**, 9171–9182 (2013)
40. J. Huang, H. Zhang, Y. Yu, Y. Chen, D. Wang, G. Zhang, G. Zhou, J. Liu, Z. Sun, D. Sun et al., Biodegradable self-assembled nanoparticles of poly (D, L-lactide-co-glycolide)/hyaluronic acid block copolymers for target delivery of docetaxel to breast cancer. Biomaterials **35**, 550–566 (2014)
41. Y. Zhu, X. Lu, X. Dong, J. Yuan, M.L. Fabiilli, X. Wang, LED-Based Photoacoustic imaging for monitoring angiogenesis in fibrin scaffolds. Tissue Eng. Part C: Methods (2019)
42. N. Sato, M.K.A. Singh, Y. Shigeta, T. Hanaoka, T. Agano, High-speed photoacoustic imaging using an LED-based photoacoustic imaging system, in *Photons Plus Ultrasound: Imaging and Sensing 2018*, vol. 10494 (International Society for Optics and Photonics, 2018), p. 104943N.
43. E. Maneas, W. Xia, M.K.A. Singh, N. Sato, T. Agano, S. Ourselin, S.J. West, A.L. David, T. Vercauteren, A.E. Desjardins, Human placental vasculature imaging using an LED-based photoacoustic/ultrasound imaging system, in *Photons Plus Ultrasound: Imaging and Sensing 2018*, vol. 10494 (International Society for Optics and Photonics, 2018), p. 104940Y
44. M.K.A. Singh, N. Sato, F. Ichihashi, Y. Sankai, In vivo demonstration of real-time oxygen saturation imaging using a portable and affordable LED-based multispectral photoacoustic and ultrasound imaging system, in *Photons Plus Ultrasound: Imaging and Sensing 2019*, vol. 10878 (International Society for Optics and Photonics, 2019), p. 108785N
45. M.K.A. Singh, T. Agano, N. Sato, Y. Shigeta, T. Uemura, Real-time in vivo imaging of human lymphatic system using an LED-based photoacoustic/ultrasound imaging system, in *Photons Plus Ultrasound: Imaging and Sensing 2018*, vol. 10494 (International Society for Optics and Photonics, 2018), p. 1049404
46. Y. Shigeta, N. Sato, M.K.A. Singh, T. Agano, Multispectral photoacoustic characterization of ICG and porcine blood using an LED-based photoacoustic imaging system, in *Photons Plus Ultrasound: Imaging and Sensing 2018*, vol. 10494 (International Society for Optics and Photonics, 2018), p. 104943O
47. S. Agrawal, C. Fadden, A. Dangi, X. Yang, H. Albahrani, N. Frings, S. Heidari Zadi, S.R. Kothapalli, Light-emitting-diode-based multispectral photoacoustic computed tomography system. Sensors **19**(22), 4861 (2019)
48. S. Agrawal, X. Yang, H. Albahrani, C. Fadden, A. Dangi, M.K.A. Singh, S.R. Kothapalli, Low-cost photoacoustic computed tomography system using light-emitting-diodes, in *Photons Plus Ultrasound: Imaging and Sensing 2020*, vol. 11240 (International Society for Optics and Photonics, 2020), p. 1124058
49. B.E. Treeby, E.Z. Zhang, B.T. Cox, Photoacoustic tomography in absorbing acoustic media using time reversal. Inverse Prob. **26**, 115003 (2010)
50. B. Wilson, G. Adam, A Monte Carlo model for the absorption and flux distributions of light in tissue. Med. Phys. **10**, 824–830 (1983)
51. L. Wang, S.L. Jacques, L. Zheng, MCML—Monte Carlo modeling of light transport in multi-layered tissues. Comput. Methods Programs Biomed. **47**, 131–146 (1995)
52. W.M. Star, Diffusion theory of light transport, in *Optical-thermal response of laser-irradiated tissue* (Springer, 1995), pp. 131–206

53. S. Agrawal, A. Dangi, N. Frings, H. Albahrani, S.B. Ghouth, S.R. Kothapalli, Optimal design of combined ultrasound and multispectral photoacoustic deep tissue imaging devices using hybrid simulation platform, in *Photons Plus Ultrasound: Imaging and Sensing 2019*, vol. 10878 (International Society for Optics and Photonics, 2019), p. 108782L
54. C. Fadden, S.R. Kothapalli, A single simulation platform for hybrid photoacoustic and RF-acoustic computed tomography. Appl. Sci. **8**, 1568 (2018)
55. G. Bal, K. Ren, On multi-spectral quantitative photoacoustic tomography in diffusive regime. Inverse Prob. **28**, 025010 (2012)
56. A. Javaherian, S. Holman, Direct quantitative photoacoustic tomography for realistic acoustic media. Inverse Prob. (2019)
57. J. Poudel, Y. Lou, M.A. Anastasio, A survey of computational frameworks for solving the acoustic inverse problem in three-dimensional photoacoustic computed tomography. Phys. Med. Biol. (2019)
58. E.M.A. Anas, H.K. Zhang, J. Kang, E. Boctor, Enabling fast and high quality LED photoacoustic imaging: a recurrent neural networks based approach. Biomed. Opt. Express **9**, 3852–3866 (2018)
59. K. Johnstonbaugh, S. Agrawal, D. Abhishek, M. Homewood, S.P.K. Karri, S.R. Kothapalli, Novel deep learning architecture for optical fluence dependent photoacoustic target localization, in *Photons Plus Ultrasound: Imaging and Sensing 2019*, vol. 10878 (International Society for Optics and Photonics, 2019), p. 449108781L
60. K. Johnstonbaugh, S. Agrawal, D.A. Durairaj, C. Fadden, A. Dangi, S.P.K. Karri, S.R. Kothapalli, A deep learning approach to photoacoustic wavefront localization in deep-tissue medium. IEEE Trans. Ultrason. Ferroelectr. Freq. Contr. (2020)